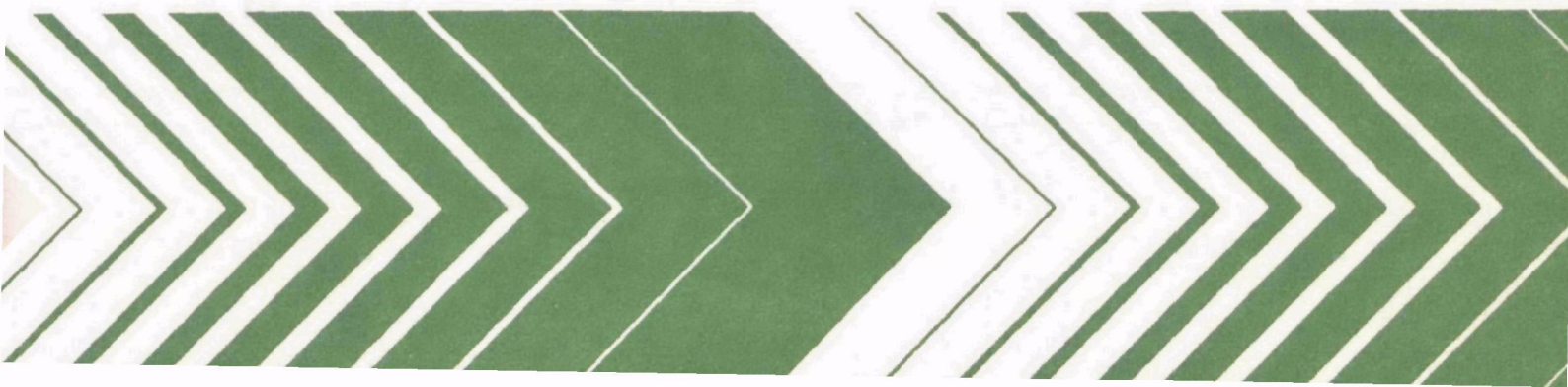


Research and Development



Enhanced Hydrodynamical- Numerical Model for Near-Shore Processes



RESEARCH REPORTING SERIES

Research reports of the Office of Research and Development, U.S. Environmental Protection Agency, have been grouped into nine series. These nine broad categories were established to facilitate further development and application of environmental technology. Elimination of traditional grouping was consciously planned to foster technology transfer and a maximum interface in related fields. The nine series are:

1. Environmental Health Effects Research
2. Environmental Protection Technology
3. Ecological Research
4. Environmental Monitoring
5. Socioeconomic Environmental Studies
6. Scientific and Technical Assessment Reports (STAR)
7. Interagency Energy-Environment Research and Development
8. "Special" Reports
9. Miscellaneous Reports

This report has been assigned to the ECOLOGICAL RESEARCH series. This series describes research on the effects of pollution on humans, plant and animal species, and materials. Problems are assessed for their long- and short-term influences. Investigations include formation, transport, and pathway studies to determine the fate of pollutants and their effects. This work provides the technical basis for setting standards to minimize undesirable changes in living organisms in the aquatic, terrestrial, and atmospheric environments.

EPA-600/3-78-073
July 1978

ENHANCED HYDRODYNAMICAL-NUMERICAL MODEL
FOR NEAR-SHORE PROCESSES

by

R. A. Bauer
and
A. D. Stroud
Compass Systems, Inc.
San Diego, California 92109

Contract Number 68-03-2225

Project Officer
R. J. Callaway
Marine and Freshwater Ecology Branch
Corvallis Environmental Research Laboratory
Corvallis, Oregon 97330

Corvallis Environmental Research Laboratory
Office of Research and Development
U. S. Environmental Protection Agency
Corvallis, Oregon 97330

DISCLAIMER

This report has been reviewed by the Corvallis Environmental Research Laboratory, U. S. Environmental Protection Agency, and approved for publication. Approval does not signify that the contents necessarily reflect the views and policies of the U. S. Environmental Protection Agency, nor does mention of trade names or commercial products constitute endorsement or recommendation for use.

FOREWORD

Effective regulatory and enforcement actions by the Environmental Protection Agency would be virtually impossible without sound scientific data on pollutants and their impact on environmental stability and human health. Responsibility for building this data base has been assigned to EPA's Office of Research and Development and its 15 major field installations, one of which is the Corvallis Environmental Research Laboratory (CERL).

The primary mission of the Corvallis Laboratory is research on the effects of environmental pollutants on terrestrial, freshwater, and marine ecosystems; the behavior, effects and control of pollutants in lake systems; and the development of predictive models on the movement of pollutants in the biosphere.

A. F. Bartsch
Director, CERL

PREFACE

The increasing concern with local environmental impacts created by various discharges into coastal waters has intensified the requirement for information regarding near-shore currents and exchange processes. A great deal of insight into near-shore dynamics can be gained through the use of sophisticated numerical tools. Simulation of processes in a numerically analogous regime can preclude learning about coastal current dynamics as the drama of a Santa Barbara oil spill engulfs beaches and birds. In the long run there is no substitute for a well-planned comprehensive direct measurement program, but planning and executing such a measurement program without the insights gained from numerical tools can prove very costly indeed.

Here the primary goal has been to extend the applications range by enhancing the capabilities of an existing numerical tool, the Hydrodynamical-Numerical (HN) model, developed by W. Hansen and T. Laevastu. As the emphasis of much earlier work was not aimed at near-shore dynamics, certain enhancements seemed in order. A secondary goal has been to more fully document the optimized HN model version, developed by R. Bauer, which provides the basis of the effort.

This report provides a more comprehensive documentation of the HN model and documents the experimental enhancements. A follow-on Users Guide will supplement this report in several important respects, namely, logic and coding details, implementation guidance and operational guidance.

ABSTRACT

An optimized version of a multilayer Hansen type Hydrodynamical-Numerical (HN) model is presented and discussed here as the basis for the following experimental extensions and enhancements developed to more appropriately handle near-shore processes:

- Non-linear term extension to facilitate small-mesh studies of near-shore, including river inflow dynamics;
- Layer disappearance extension to enable appropriate procedures in tidal flat and marshy regions, as well as some down/upwelling cases;
- Thermal advection enhancement for treatment of thermal pollution cases by method of moments coupled with heat budget procedures for dynamic plume development experiments;
- Monte Carlo diffusion enhancement to deal with dispersion via statistical methods and comparison to the method of moments experiments.

Extensive efforts were invested in determining reasonable and appropriate boundary conditions for both the basic model and the extended versions presented here.

This report was submitted in fulfillment of contract No. 68-03-2225 by Compass Systems, Inc. under the sponsorship of the U. S. Environmental Protection Agency. This work covers the period from June 1975 to March 1977 and was completed March 31, 1977.

CONTENTS

Foreword	iii
Preface.	iv
Abstract	v
Figures.	viii
Tables	ix
Abbreviations and Symbols.	x
Acknowledgment	xiii
1. Introduction	1
2. Conclusions and Recommendations.	2
3. Numerical Methods and Techniques	4
4. Experimental Extensions of the HN Model.	20
5. Results and Discussion	31
References	46
Appendix	
A. Verification of the Model.	49

FIGURES

<u>Number</u>		<u>Page</u>
1	Scheme of the numerical grid.	6
2	Orientation of the numerical grid	7
3	\bar{U}^* , ζ (other than $\bar{\zeta}$), and \bar{V}^* computational stencils at closed boundaries	12
4	U , V computational stencils at open boundaries.	12
5	ζ and $\bar{\zeta}$ computational stencils at open boundaries	13
6	\bar{U}^* , \bar{V}^* computational stencils at open boundaries.	13
7	\bar{U} , \bar{V} computational stencils at open boundaries.	14
8	$\bar{\zeta}$, \bar{U} , \bar{V} computational stencils at closed boundaries	15
9	Fractional z index notation	20
10	U , V non-linear computational stencils at closed boundaries . .	22
11	U , V non-linear computational stencils at open boundaries . . .	23
12	The (n,m) cell.	24
13	h_u depth profile for coastal grid	31
14	Tidal flat grid	32
15	Tidal flat grid bathymetry (depths in cm)	33
16	Closure configuration TFC: $t=17700$ sec.	40
17	Closure configuration TFC: $t=18090$ sec.	40
18	Closure configuration TFC: $t=18240$ sec.	41
19	Closure configuration TFC: $t=18390$ sec.	41
20	Closure analysis for TFC cell $(6, 13)$	42

<u>Number</u>		<u>Page</u>
21	Post-reopening analysis for TFC cell (6, 13).	42
22	Maximum seaward advance of tidal flat F234.	43
23	TFC continuous source "plumes".	45
A-1	San Onofre outfall area grid bathymetry	50
A-2	San Onofre outfall tidal and wind prescription August 2, 1972 .	51
A-3	Infrared flight 0958-1107 compared to values after 15 source hours.	53
A-4	Infrared flight 1226-1344 compared to values after 17 source hours.	53
A-5	Infrared flight 1503-1617 compared to values after 19 source hours.	54

TABLES

<u>Number</u>		<u>Page</u>
1	Boundary Condition Confusion.	11
2	Typical Tidal Flat Grid and Run Specifications.	34
3	Flat F3 Formation; Non-linear vs Linear	36
4	Flat F4 Formation; Non-linear vs Linear	37
5	Flat F1 Formation; Non-linear vs Linear	38
6	Flat F2 Formation; Non-linear vs Linear	39

LIST OF ABBREVIATIONS AND SYMBOLS

ABBREVIATIONS

F1-F4	--bathymetric features identified by notes 1 - 4 on Figure 14; also tidal flat segments associated with bathymetric features
F1234	--tidal flat associated with combined features F1-F4
F234	--tidal flat associated with combined features F2-F4
F34	--tidal flat associated with combined features F3 and F4
HN	--Hydrodynamical-Numerical
I	--the array index $(n,m)=(m-1)NE+n$
m,M	--the column index $(m=1,2,\dots,ME-1,ME)$
MM	--the array index $(n,m-1)=I-NE(m \text{ minus})$
MP	--the array index $(n,m+1)=I+NE(m \text{ plus})$
n,N	--the row index $(n=1,2,\dots,NE-1,NE)$
NE	--number of rows for array variables
NM	--the array index $(n-1,m)=I-1(n \text{ minus})$
NMMP	--the array index $(n-1,m+1)=I+NE-1(n \text{ minus}, m \text{ plus})$
NP	--the array index $(n+1,m)=I+1(n \text{ plus})$
NPMM	--the array index $(n+1,m-1)=I-NE+1(n \text{ minus}, m \text{ plus})$
TFC	--Tidal Flat Convective (nonlinear tidal flat case)

SYMBOLS

A	--area variable
An	--noon altitude of the sun in degrees
Aw	--ambient water temperature
c	--cloudiness factor in tenths of the sky
\bar{c}	--mean specific heat
C	--conservative quantity (concentration or volume)
d	--depth (thickness) of the heated fluid
Ea	--moist vapor pressure of air
Ew	--saturation vapor pressure of air
f	--coriolis parameter
F	--center of concentration (one dimensional case)
Fx,Fy	--x,y coordinates of center of conservative quantity
g	--acceleration of gravity
h	--initial layer thickness
H	--dynamic layer thickness
\bar{H}	--mean thickness at z point
i	--layer indicator $(i=1,k)$
j	--general index
k	--number of layers in the HN model
K	--new heat quantity (added heat)

M_0 --zeroth order moment of conservative quantity
 M_1 --first order moment of conservative quantity
 M_2 --second order moment of conservative quantity
 \sim
 N --a unit vector normal to the indicated boundary
 p --stochastic variate
 P --population of stochastic variates
 q_L --effect of external sources on layer surface deviation
 Q --net heat flux
 Q_b --net atmospheric-oceanic (long wave) radiative heat flux
 Q_e --evaporative/condensative heat flux
 Q_h --net atmospheric-oceanic sensible heat flux (convective transfer or conduction)
 Q_m --heat flux resulting from human efforts
 Q_r --reflected (short wave) radiative heat flux
 Q_s --total incident
 Q_{os} --total clear sky incident (short wave) radiative heat flux
 r --friction coefficient
 R --width of a conservative quantity or a random value between zero and one
 R_x, R_y --x,y widths of a conservative quantity
 s --distance variable
 S --stochastic coefficient
 t --time variable
 t_d --length of a day (sunrise to sunset in minutes)
 t_0 --initial time (start of a computation)
 T --temperature variable
 \sim
 \hat{T} --unit vector in the tangential direction
 T_a --surface air temperature
 T_w --mean surface water temperature for a cell
 u, v --indicators of points of computation for U and V, respectively
 $u[P], v[P]$ --u,v turbulence component assigned the value of p
 U, V --vertically integrated velocity components for the x,y direction, respectively
 $\overline{U}, \overline{V}$ --the "smoothed" U and V components, respectively (result of eddy viscosity)
 $^{*} \ ^{*}$
 U, V --linearly interpolated u,v velocity components at the u,v points, respectively
 U_0 --relative humidity (%)
 W --wind speed (m/sec)
 x, y --horizontal space coordinate variables
 X, Y --horizontal components in the x,y direction, respectively, of external forces including the air-sea interface
 z --indicator of points of computation for ζ

α --smoothing parameter
 $\bar{\alpha}$ --the mean altitude of the sun for a short period
 δ --directional parameter
 ϵ --directional parameter
 l --half grid length
 τ --half time step
 ρ --density of fluid (assumed uniform through layer)
 ζ --deviation of the top of the layer from an arbitrary level surface
 $\bar{\zeta}$ --smoothed value of ζ (result of eddy diffusivity)
 \tilde{v} --vector velocity (resultant of U and V)
 \cdot --vector "dot" product
 \cdot --superscript dot represents the operator $\partial/\partial t$
 $|$ --interpreted as "evaluated on"
 ∂N --an element of the normal to the indicated boundary
 $()_x$ --represents the operator $\partial/\partial x$
 $()_y$ --represents the operator $\partial/\partial y$
 ∇^2 --represents the operator $\partial^2/\partial x^2 + \partial^2/\partial y^2$
 Δ --the difference analog to ∂
 \approx --"approximately equal to"
 ∇ --represents the vector operator $\tilde{i}\partial/\partial x + \tilde{j}\partial/\partial y$ (where \tilde{i} and \tilde{j} represent unit normal vectors in the x,y direction, respectively)

ACKNOWLEDGMENTS

We wish to thank the Naval Environmental Prediction Research Facility for allowing use of their facilities; S. Larson, K. Rabe and J. Harding for their many constructive suggestions; and the NPERF computer support personnel for their assistance.

We wish to thank Dr. T. Laevastu for his guidance and to acknowledge all of his innovative enhancements to the original Hansen model, which formed the basis for the optimized model.

We wish to express our appreciation to R. Callaway, Project Officer, for providing the proper environment to perform theoretical studies of the model and wish to note the thoughtful user oriented feedback from C. Koblinkski, also of the Corvallis laboratory.

Finally, we wish to express our thanks to S. Haines for preparing the illustrations and tables and to D. Bauer for typing the report.

SECTION 1

INTRODUCTION

The Hansen type optimized multilayer Hydrodynamical-Numerical (HN) model described by Bauer (1) is a practical tool which has been used successfully to study the dynamics of numerous coastal areas. The optimized version of the HN model combines the vertically integrated single layer HN model originally developed by Professor W. Hansen (2), (3), University of Hamburg, Germany, and the multilayer multiple-open boundary HN model proposed by Hansen and developed by Dr. T. Laevastu (see Laevastu, et al., (4)-(9)).

The thrust of much prior development of the HN model was toward large coastal areas, semi-enclosed seas and even open ocean areas. In order to adequately focus the model on near-shore problems certain enhancements were required. First, non-linear terms of the dynamical equations not essential for much earlier work are required for near-shore scales of motion. Second, layer disappearance problems, tidal flats and marshes, for example, handled inadequately by prior versions of the model, required proper treatment in near-shore cases. Additionally, evaluation and extension to thermal advection problems, as well as Monte Carlo dispersion procedures, were deemed essential to show the utility of the numerical model procedure in practical applications.

SECTION 2

CONCLUSIONS AND RECOMMENDATIONS

The non-linear (convective) term modifications have been successfully implemented in the single layer optimized version of the HN model and should be incorporated whenever an HN application is expected to have significant current gradients. Experience indicates that the non-linear terms do not play a significant role when the grid length in the difference scheme exceeds one kilometer. When the grid length is less than one kilometer, however, current gradients tend to make the non-linear terms significant. The non-linear modifications as developed were designed for multiple layer applications (from one to three layers in the current version) and should present no difficulties when applied to multilayer cases. No testing has been performed for any multilayer case, however.

The "tidal flat" modifications have been successfully implemented in the surface layer and are practicable for inclusion in any HN application where layer disappearance phenomena are an essential feature of the dynamics. Use of these modifications would generally imply use of the non-linear terms as well. The multilayer case was designed to handle multilayer disappearance problems, e.g., down/upwelling through an initially extant layer. Again, no extensive testing of the multilayer feature has been performed and some important upwelling cases are not handled adequately, e.g. extension of a lower layer horizontally into a region where the layer was not initially extant. These latter cases were not covered due to basic model design change requirements.

Coupling of the heat budget formulation with the conservative duplex advection of "added heat" and volume of heated fluid has been successful within the assumptions made. Verification with a real case would be desirable to validate the procedural verification. The assumption of advection without diffusion is somewhat restrictive, thus experiments toward inclusion of a controlled diffusive scheme would be desirable. The method solves the practical problem in its present form, but could be improved as to display of temperature anomaly fields.

The Monte Carlo technique compares quite favorably to the conservative advection by method of moments in terms of quantitative results. For test cases, the cost of the Monte Carlo procedure was roughly an order of magnitude less than the method of moments for approximately comparable quantitative resolution with the same temporal resolution. The cost of any Monte Carlo method is proportional to the statistical sample size, where the cost of the method of moments is proportional to the number of affected grid cells.

The present work included only procedural verification of the extensions and enhancements. No attempt has been made to simulate any particular real

case for comparison with real data sources. Verification of this latter type should be accomplished prior to any attempt at predicting a real case using these experimental procedures.

Various subtle aspects of the HN model and its associated boundary conditions should be investigated further. For example, a tangential free slip condition may enhance computations near unprescribed open boundaries by reducing the transverse frictional effects currently associated with these artificial grid bounds.

SECTION 3

NUMERICAL METHODS AND TECHNIQUES

THE HYDRODYNAMICAL-NUMERICAL MODEL

The Hydrodynamical-Numerical (HN) model is an explicit numerical difference scheme based on leap-frog integration of the two dimensional Eulerian form of the hydrodynamical equations through time to obtain a dynamical boundary-value solution of tidal order.

The Hydrodynamical Equations

The following differential form of the hydrodynamic equations was derived by integration of both x and y velocity components through a layer of assumed uniform density to achieve vertically averaged mean components. Terms to account for rotation of the earth, wind and tidal forcing, and dissipative bottom (and upper layer) frictional effects have been included. In multilayer cases the dissipative frictional effects are grossly represented in upper layers as 50% of that which would have been computed for a bottom layer of the same velocity/depth configuration. A more physically realistic interlayer friction term would consider velocity in adjacent layers as stress transferring momentum between layers as well as slightly dissipating mechanical energy (to heat) within each layer. Eddy viscosity/diffusivity terms have been omitted, as their use is more intimately related to numerical schemes than to any imperative of physics. (See section on numerical smoothing below.) Leendertse (10) provides a relatively detailed development and analysis of the essential form of the differential equations presented here. The form is analogous to that presented by Hansen (2), (3) and is substantially the same as that presented by Laevastu (7), (11) and (14).

These equations for layer i of k layer system (where i=1 in the surface layer) are as follows:

Continuity:

$$\dot{\zeta}_i - \dot{\zeta}_{i+1} + (H_i U_i)_x + (H_i V_i)_y = q_L \quad (1)$$

x Momentum:

$$\begin{aligned} \dot{U}_i + U_i (U_i)_x + V_i (U_i)_y - f V_i + r_i (U_i^2 + V_i^2)^{.5} H_i^{-1} U_i \\ + g \left(1 - \frac{\rho_{i-1}}{\rho_i}\right) (\zeta_i)_x + g \left(\frac{\rho_{i-1}}{\rho_i}\right) (\zeta_{i-1})_x = x_i, \end{aligned} \quad (2)$$

y Momentum:

$$\begin{aligned} \dot{V}_i + U_i (V_i)_x + V_i (V_i)_y + f U_i + r_i (U_i^2 + V_i^2)^{.5} H_i^{-1} V_i \\ + g \left(1 - \frac{\rho_{i-1}}{\rho_i}\right) (\zeta_i)_y + g \left(\frac{\rho_{i-1}}{\rho_i}\right) (\zeta_{i-1})_y = y_i \end{aligned} \quad (3)$$

where:

- ζ --deviation of the layer surface from an arbitrary level,
- U, V --horizontal components in the x,y direction, respectively, of the vertically integrated velocity,
- H --thickness of the layer,
- x, y --horizontal space coordinate variables,
- X, Y --horizontal components in the x,y direction, respectively, of the external forces at the air-sea interface,
- f --coriolis parameter,
- r --friction coefficient,
- g --acceleration of gravity,
- ρ --density of the medium,
- q_L --effect of external sources such as river inflow and rainfall on layer surface deviation;

the following notational conventions apply:

- "." --represents the operator $\partial/\partial t$ (superscript dot),
- $()_x$ --represents the operator $\partial/\partial x$,
- $()_y$ --represents the operator $\partial/\partial y$;

and the following conditions at upper or lower fluid boundaries apply:

$$\dot{\zeta}_{i+1} = 0, \text{ when layer } i \text{ intersects bottom topography,}$$

$$(\zeta_{i-1})_x = (\zeta_{i-1})_y = \rho_{i-1} = 0, \text{ when } i=1.$$

Numerical Difference Scheme

Computational Grid--

The finite difference equations presented in the following sub-section are based on the staggered grid shown in Figure 1. The z grid points (intersections of grid net) identify the geographic positions where ζ values are computed. The u grid points are one-half a grid length to the right of the correspondingly indexed z grid points. The v grid points are one-half a grid length below correspondingly indexed z grid points. Computation of U and V velocity components occur at u and v grid points, respectively. Positive U and V velocity components are directed to the right and upward, respectively, in Figure 1. The relationship between computational coordinates and geographic coordinates is established by Figure 2. All land or sea features must contain at least one z grid point. In particular, at least one z grid point must separate an open boundary from a parallel closed boundary. The last v row and the last u column become superfluous in the computational scheme but are required for proper initialization.

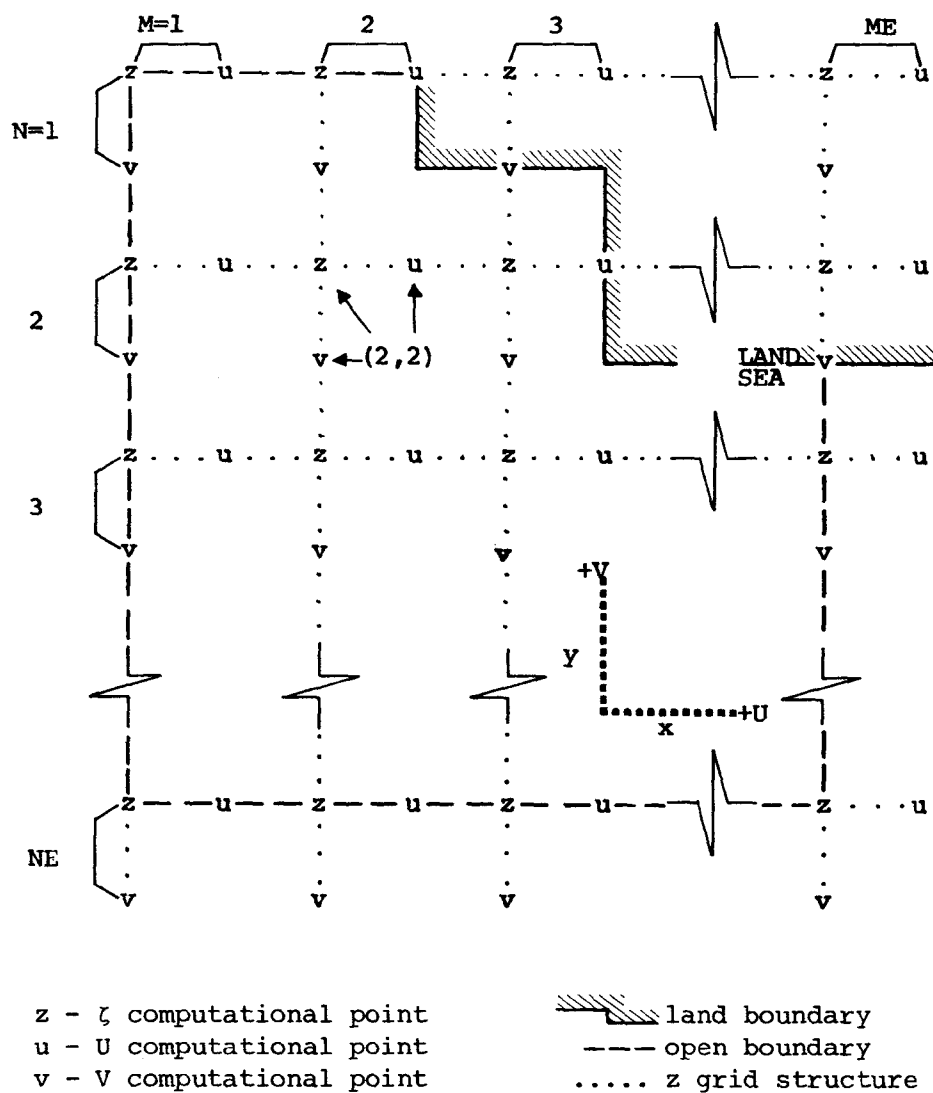


Figure 1. Scheme of the numerical grid.

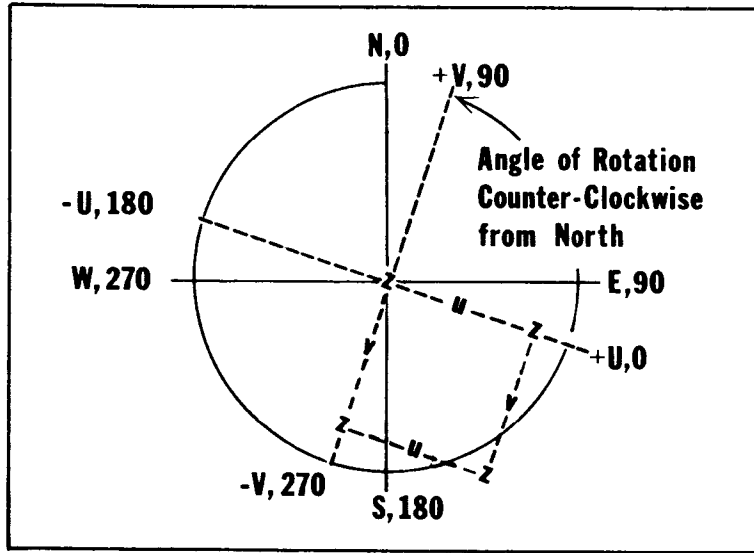


Figure 2. Orientation of the numerical grid.

The grid point indexing convention used in Hansen models is for the z grid intersection, the u point to the right and the v point below, to have the same double subscripts with the row index first. The row index is $n:1 \leq n \leq NE$ and the column index is $m:1 \leq m \leq ME$. In the optimized model the convention is retained; however, a single index $(I)=(n,m)$ is defined and is computed using FORTRAN array subscript convention, as $I=(m-1)*NE+n$. (Columns are stored by consecutive elements; arrays are stored by consecutive columns.) The following additional indexing abbreviations are used:

MM --index $(n,m-1)=I-NE=m$ minus
 MP --index $(n,m+1)=I+NE=m$ plus
 NM --index $(n-1,m)=I-1,n$ minus
 NP --index $(n+1,m)=I+1=n$ plus
 NPM --index $(n+1,m-1)=I+1-NE=n$ plus, m minus
 NMMP --index $(n-1,m+1)=I-1+NE=n$ minus, m plus

Finite Difference Form of the Equations--

The finite difference form of Equations 1-3 that follow are essentially the same as in W. Hansen's single layer model except the terms dictated by the presence of k layers are added and the convective terms usually omitted in the basic model have been included. Symbols are as previously defined except as noted. The k layer model is:

$$\begin{aligned} \zeta_i^{t+\tau}(I) = & \zeta_i^{t+\tau}(I) - (\tau/\ell) \sum_{j=i,k} \{ Hu_j^{t-\tau}(I) U_j^t(I) - Hu_j^{t-\tau}(MM) U_j^t(MM) \\ & + H V_j^{t-\tau}(NM) V_j^t(NM) - H V_j^{t-\tau}(I) V_j^t(I) \} + 2\tau q_L; \end{aligned} \quad (4)$$

$$\begin{aligned}
U_i^{t+2\tau}(I) = & \bar{U}_i^t - \{ [2\tau r_i / Hu_i^{t+\tau}(I)] [U_i^t(I)^2 + V_i^{*t}(I)^2]^{.5} \} U_i^t(I) + 2\tau f \bar{V}_i^{*t}(I) \\
& - .5(\tau/\ell) \{ [U_i^t(MP) - U_i^t(MM)] U_i^t(I) + [U_i^t(NM) - U_i^t(NP)] \bar{V}_i^{*t}(I) \} \\
& - g(\tau/\ell) \{ [1 - (\rho_{i-1}/\rho_i)] [\zeta_i^{t+\tau}(MP) - \zeta_i^{t+\tau}(I)] \\
& + (\rho_{i-1}/\rho_i) [\zeta_{i-1}^{t+\tau}(MP) - \zeta_{i-1}^{t+\tau}(I)] \} + 2\tau X_i^{t+\tau}(I); \quad (5)
\end{aligned}$$

$$\begin{aligned}
V_i^{t+2\tau}(I) = & \bar{V}_i^t - \{ [2\tau r_i / Hv_i^{t+\tau}(I)] [V_i^t(I)^2 + U_i^{*t}(I)^2]^{.5} \} V_i^t(I) - 2\tau f \bar{U}_i^{*t}(I) \\
& - .5(\tau/\ell) \{ [V_i^t(NM) - V_i^t(NP)] V_i^t(I) + [V_i^t(MP) - V_i^t(MM)] U_i^{*t}(I) \} \\
& - g(\tau/\ell) \{ [1 - (\rho_{i-1}/\rho_i)] [\zeta_i^{t+\tau}(I) - \zeta_i^{t+\tau}(NP)] \\
& + (\rho_{i-1}/\rho_i) [\zeta_{i-1}^{t+\tau}(I) - \zeta_{i-1}^{t+\tau}(NP)] \} + 2\tau Y_i^{t+\tau}(I); \quad (6)
\end{aligned}$$

where:

$$\begin{aligned}
\bar{U}(I) &= \alpha U(I) + .25(1-\alpha) [U(NM) + U(NP) + U(MM) + U(MP)], \\
\bar{V}(I) &= \alpha V(I) + .25(1-\alpha) [V(NM) + V(NP) + V(MM) + V(MP)], \\
\bar{\zeta}(I) &= \alpha \zeta(I) + .25(1-\alpha) [\zeta(NM) + \zeta(NP) + \zeta(MM) + \zeta(MP)]; \quad (7)
\end{aligned}$$

$$\begin{aligned}
\bar{U}^*(I) &= .25 [U(I) + U(NP) + U(MM) + U(NPMM)], \\
\bar{V}^*(I) &= .25 [V(I) + V(NM) + V(MP) + V(NMMP)]; \quad (8)
\end{aligned}$$

$$\begin{aligned}
Hu_i^{t+\tau}(I) &= hu_i + .5 \{ [\zeta_i^{t+\tau}(I) + \zeta_i^{t+\tau}(MP)] - [\zeta_{i-1}^{t+\tau}(I) + \zeta_{i-1}^{t+\tau}(MP)] \}, \\
Hv_i^{t+\tau}(I) &= hv_i + .5 \{ [\zeta_i^{t+\tau}(I) + \zeta_i^{t+\tau}(NP)] - [\zeta_{i+1}^{t+\tau}(I) + \zeta_{i+1}^{t+\tau}(NP)] \}; \quad (9)
\end{aligned}$$

where:

- h --initial layer thickness,
- t --time variable,
- u,v --indicators of U and V computational points, respectively,
- ℓ --half grid step,
- α --smoothing parameter,
- τ --half time step.

Numerical Smoothing--

Explicit solution of non-linear systems requires systematic suppression of the shortest waves through smoothing or other techniques to avoid non-linear instability. Equations 7 (the "bar" terms) introduced numerical smoothing into the difference solution. The differential form of these terms was not made explicit, since their introduction into the difference form is a numerical device, rather than a physically necessary term.

Smoothing techniques have been applied to hydrodynamic models to suppress higher order harmonic waves generally associated with non-linear

instability. Lamb (13) applied a successive approximation analysis to the simplified non-linear differential system:

$$\begin{aligned}\dot{U} + U(U)x &= -g(\zeta)x, \\ \dot{\zeta} &= -[(h+\zeta)U]x.\end{aligned}\tag{10}$$

He demonstrated the appearance of higher order harmonics in the analytic solution of this non-linear system. Successively higher order harmonics are introduced at each step, limited in the difference solution by the minimum representable wavelength. Energy is thus transferred from longer to shorter waves and is accumulated in the shortest possible waves. Leendertse (10) showed that the transferred energy becomes fixed in space due to the zero velocity associated with the shortest waves.

The bar terms imply an "artificial viscosity or diffusivity" term in the differential form. The artificial term in each momentum equation has been interpreted physically as "horizontal or lateral eddy viscosity or turbulent friction." These terms would appear on the right-hand side of Equations 2 and 3 as $+Ai\nabla^2 U_i$ and $+Ai\nabla^2 V_i$, respectively, where ∇^2 is the two dimensional Laplacian operator: $\partial^2/\partial x^2 + \partial^2/\partial y^2$. The form of the analytic solution according to Lamb (13) shows the requirement for a corresponding "lateral eddy diffusivity" term which would appear on the right-hand side of Equation 1 as $Ai\nabla^2 \zeta_i$. The coefficients of these "artificial viscosity and diffusivity"

terms become in the difference form $(1-\alpha_i)\ell^2/2$, where α_i is an arbitrary smoothing parameter, usually chosen near .99. These artificial terms have been retained as a tuning factor in many quasi-linear HN applications, e.g., Hansen (3), Laevastu (4)-(9), (11), (12) and (14). The smoothing parameter should most properly be a function of the horizontal eddy viscosity/diffusivity coefficient and the grid/time step to avoid arbitrarily heavy smoothing with resultant misleading dynamic impacts.

An interesting sidelight to the smoothing problem is the smoothing inherent in the scheme through linear interpolation. Particularly with reference to the star terms (\bar{U}, \bar{V}) , Kagan (15) states that the HN system "will lead to extremely strong smoothing in the calculated velocities and elevations." His analysis reveals that for a grid mesh length in excess of about 30 Km the "computational viscosity" coefficient would exceed that expected for horizontal turbulence in tidal motion. This should be a topic of further study; however, it is doubtful that the "computational viscosity" inherent in the star term would replace the smoothing required for non-linear model stability.

Boundary Conditions

Differential Form--

The area of interest is defined by an enclosing boundary (Γ), which includes open and closed boundary segments. The boundary conditions which are applied at the land-sea (closed) boundary (Γ_1) and the sea-sea (open) boundary (Γ_2) in a differential form are:

$$\text{Condition 1:} \quad \tilde{v} \cdot \tilde{N}|_{\Gamma_1} = 0, \tag{11}$$

$$\text{Condition 2:} \quad \zeta|_{\Gamma_2} = \zeta(x,y,t), \quad (12)$$

$$\text{Condition 3:} \quad \partial(\tilde{v} \cdot \tilde{N}) / \partial N|_{\Gamma_2} = 0, \quad (13)$$

$$\text{Condition 4:} \quad \partial H / \partial N|_{\Gamma_2} = 0, \quad (14)$$

$$\text{Condition 5:} \quad \partial \zeta / \partial N|_{\Gamma} = 0, \quad (15)$$

$$\text{Condition 6:} \quad \partial(\tilde{v} \cdot \tilde{T}) / \partial N|_{\Gamma} = 0, \quad (16)$$

where:

\tilde{v} --vector velocity,
 \tilde{N} --a unit vector normal to the indicated boundary,
 \tilde{T} --a unit vector tangential to the indicated boundary,
 $"."$ --vector "dot" product,
 $|$ --may be interpreted as "evaluated on",
 ∂N --an element of the normal to the indicated boundary.

(Note that $\tilde{v} \cdot \tilde{T} = U$ and $\tilde{v} \cdot \tilde{N} = V$ along a boundary in the x direction and vice versa along a boundary in the y direction.) Conditions 1 and 2 are Dirichlet conditions, while conditions 3 through 6 are Neuman conditions. The combination of conditions applied may be viewed as a Cauchy condition, which is precisely the required condition for hyperbolic systems of equations.

The combination of conditions 1, 3 and 6 form a Cauchy condition on the velocity variables. The combination of conditions 2 and 5 form a Cauchy condition on the ζ variable. Condition 4 is required only in association with condition 2 when $\zeta(x,y,t)$ is computed dynamically. TABLE 1 shows the conditions and their effect.

Condition 1 effects land-sea boundary closure by imposing zero normal velocity at the boundary. Tidal harmonics, permanent flow characteristics, river inflow characteristics, etc., are generally imposed via condition 2. Condition 3 establishes a uniform velocity condition at the open boundary only. This differs from the work of Kagan (15), which suggested application only at closed boundaries. Since only one condition may be applied at any given boundary node, the no-flow condition, Equation 11, was chosen for all closed normal boundaries.

When condition 2 is not applied via external information, conditions 4 and 5 complement condition 3 to form in concert a uniform flow condition at open boundaries. Condition 5 at closed boundaries was selected to effect a slight amplitude gradient damping, while avoiding a laminar or quasi-laminar amplitude damping. Condition 6 implies a slip condition along both open and closed tangential boundaries. In an extremely fine mesh model a laminar (infinite lateral friction; zero slip) condition might be indicated. The gross scale of HN applications indicates, however, that slight velocity gradient damping, Equation 16, is sufficient at land-sea and open boundaries.

Difference Method of Applications--

The various methods of applying in the difference scheme conditions 1-6 specified in Equations 11-16 are presented in this section with figures for clarification. Figures 3-8 depict computational stencils, which enclose geographic positions for values required by the indicated computations.

TABLE 1: BOUNDARY CONDITION CONFUSION

BOUNDARY CONDITION			BOUND TYPE	DIFFERENCE ORDER OF APPROX.	COMPUTATION DIRECTLY AFFECTED	BOUNDARY CONDITION TYPE; FRICTIONAL EFFECT	DIFFERENCE METHOD OF EFFECT-ING BOUNDARY CONDITION
#	Eq.	Fig.					
1	(11)	3,8	closed	1st	$\zeta, \bar{U}, \bar{V}, \bar{U}^*, \bar{V}^*$	Solid wall, zero normal flow; infinite normal friction	Zero normal velocity compon-ent effects land-sea closure
		10	Γ_1	2nd	non-linear terms		
2	(12)	4	open Γ_2	1st	H_u, H_v, U, V, ζ	External forcing	Tidal harmonic/permanent flow/river inflow/"overtide" specification
		5				Internal dynamic	Values not specified comput-ed dynamically under Condi-tions 3,4,5
3	(13)	5,6,7	open Γ_2	1st	$\bar{U}^*, \bar{V}^*, \bar{U}, \bar{V}, \zeta$	Reflective condition with phase shift due to light (1st order) or moderate (2nd order) friction effecting damping of gradient normal to indicated boundary	Index modification effects value assignment such that same computational form may be used for both internal and boundary computations
		11		2nd	nonlinear terms		
4	(14)	5	open Γ_2	1st	ζ		
5	(15)	5	open Γ_2	1st	$\bar{\zeta}$		
		8	closed Γ_1			Reflective condition with phase shift due to light friction effect-ing damping of gradient normal to indicated boundary	
6	(16)	8	closed Γ_1	1st	\bar{U}, \bar{V}	Perfect transverse re-flection, total slip, zero friction.	A combination of value and index modification allows the same form to be used for both internal and boundary compu-tations
		7	open Γ_2				
7	(33)	11	open Γ_2	2nd	nonlinear terms		Extrapolation of internal transverse gradient (doubl-ing of first order half dif-ference computed due to in-dex modification.)
		10	closed Γ_1				

Superscript numerals in these figures identify the numbered boundary conditions that are applied. Arrows where shown in Figures 3-8 indicate effective value transfer used to impose the boundary conditions.

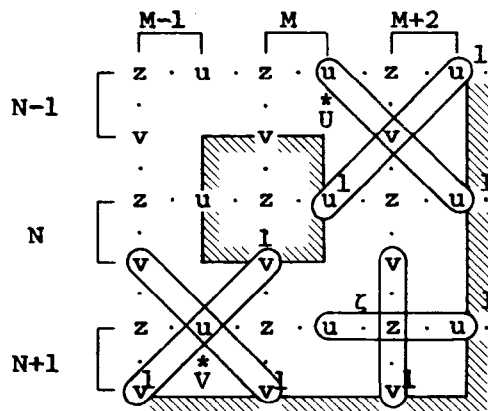


Figure 3. \bar{U} , ζ (other than $\bar{\zeta}$), and \bar{V} computational stencils at closed boundaries.

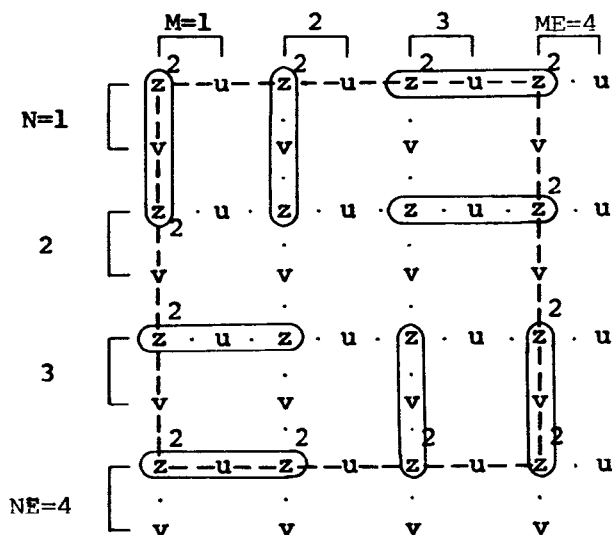


Figure 4. U , V computational stencils at open boundaries.

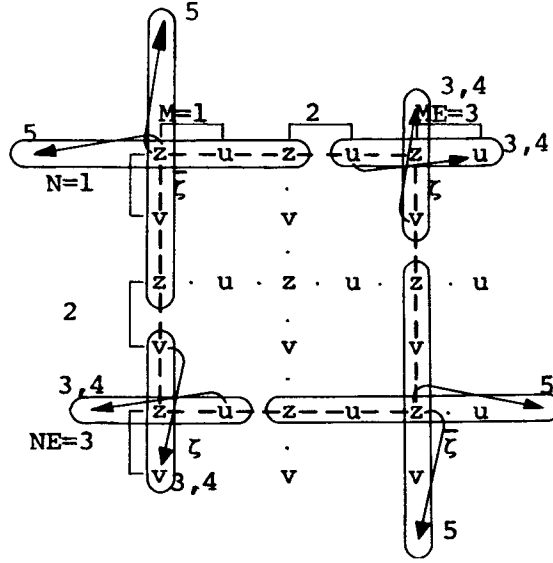


Figure 5. ζ and $\bar{\zeta}$ computational stencils at open boundaries.

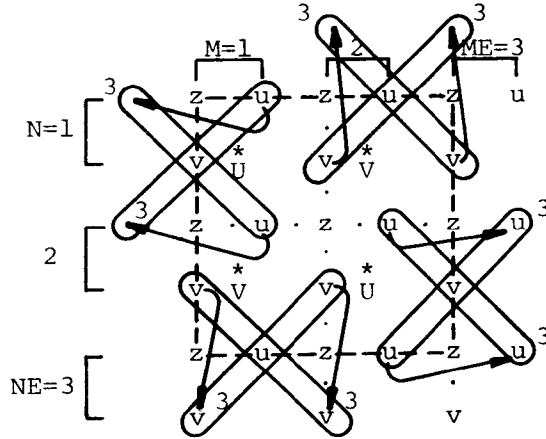


Figure 6. \bar{U}^* , \bar{V}^* computational stencils at open boundaries.

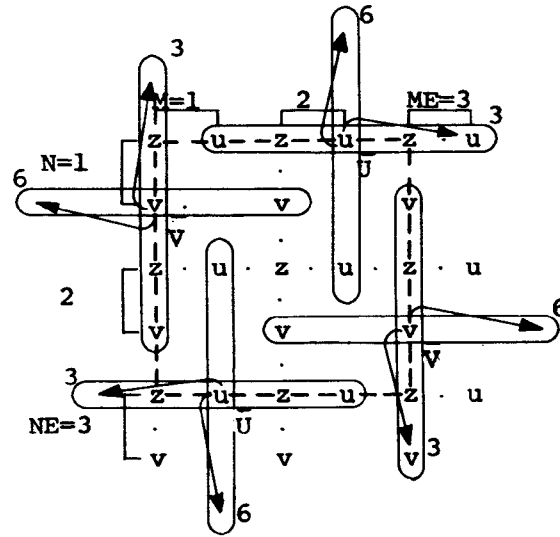


Figure 7. \bar{U} , \bar{V} computational stencils at open boundaries.

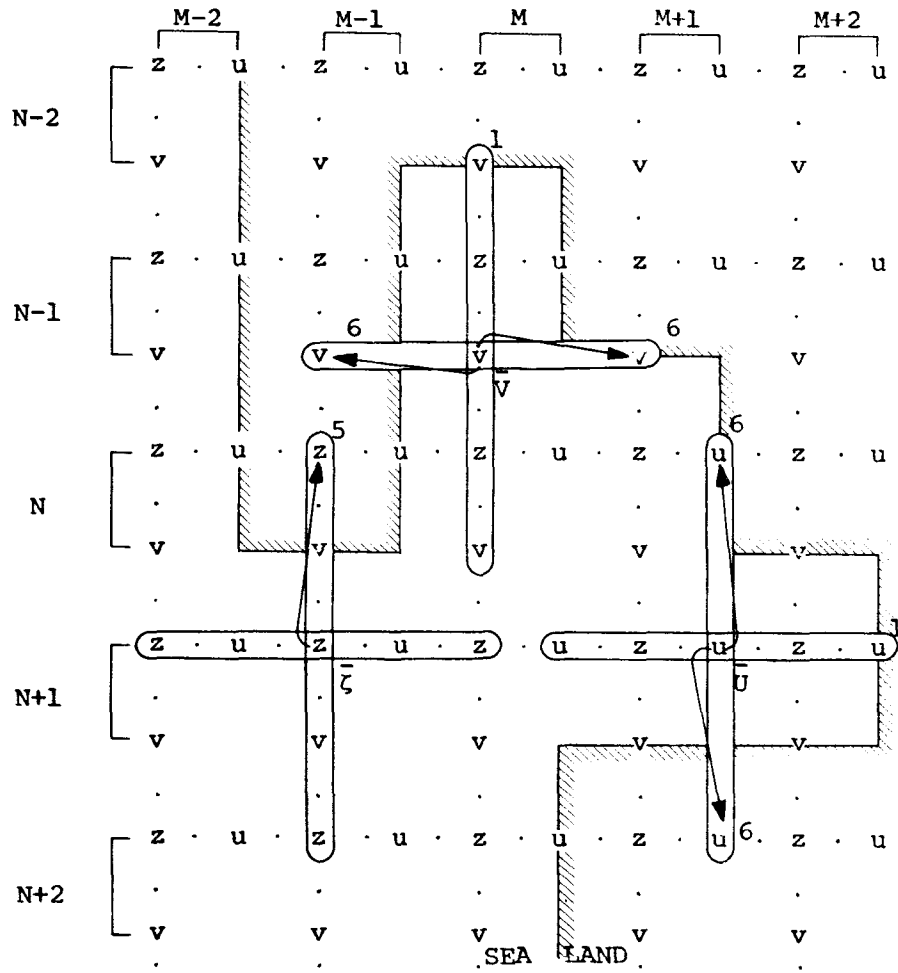


Figure 8. $\bar{\zeta}$, \bar{U} , \bar{V} computational stencils at closed boundaries.

Condition 1 at closed bounds--By definition of the grid structure, land-sea boundaries are associated with positions of zero depth. Velocity components associated with zero depth values are initialized and remain equal to zero. As a result, Equation 11 is satisfied in the difference scheme without modification of the derived difference forms adjacent to normal land-sea boundaries: the zero velocity components on land-sea boundaries are simply used for computations of $\bar{\zeta}$, \bar{U}^* , \bar{V}^* , \bar{V} , \bar{U} as required. (Refer to positions identified by superscript 1 in Figures 3 and 8.)

Condition 2 at open bounds--Equation 12 is satisfied in the difference scheme by providing $\bar{\zeta}$ values from external information, where available, or by computing a dynamic $\bar{\zeta}$ value constrained by conditions 3-5. (Refer to positions identified by superscript 2 in Figure 4.)

Conditions 3-6 at open bounds--Equations 13-16 are satisfied in the difference scheme at open boundaries such that values representing a position: (1) outside the defined grid mesh, (2) in the last row of V, hv or Hv values or (3) in the last column of U, hu or Hu values, are replaced with the next like variable value lying on an inward directed normal line from the intervening boundary. (Refer to positions identified by superscript 3-6 in Figures 5-7.)

Conditions 5 and 6 at closed bounds--Equations 15 and 16 are satisfied in the difference scheme at closed boundaries such that values representing positions over land (or at a normal boundary not intersected by the tangential flowline) are replaced with the next like variable value lying on the seaward directed normal line from the intervening tangential boundary. (Refer to positions identified by superscripts 5 and 6 in Figure 8.)

ADVECTION BY METHOD OF MOMENTS

The method of moments is a quasi-Lagrangian method which maintains information on the zeroth, first and second order moments of the concentration in each cell of the grid mesh. The scheme preserves concentration gradients in the original distribution through time based on externally supplied advection velocities while avoiding the pseudo-diffusion encountered in Eulerian difference methods.

The method selected for use here is that of Pedersen and Prahm (16). The differential equation of advection $\partial C/\partial t = -V \cdot \nabla C$, holds where C is any conservative quantity, as long as V is a non-divergent velocity field. HN integrated velocities (vertically averaged) over a region of variable depth do not precisely satisfy the non-divergence requirement. It has been assumed that for the regions of interest these divergence effects will not be significant. A single Lagrangian step is taken based on a velocity at the point interpolated from the Eulerian grid. Immediately the parameters of interest are decomposed from the results of the Lagrangian step back into the Eulerian framework by summation of contributions from surrounding cells. The parameters of interest for each cell are total conservative quantity C, center of concentration F and width of the quantity R. The equations used for the zeroth, first and second order moments in one dimension are:

$$M_0 = C = \int_{-.5}^{+.5} C(x) dx, \quad (17)$$

$$M_1 = F = \int_{-.5}^{+.5} C(x) x dx / C, \quad (18)$$

$$M_2 = R^2/12 = \int_{-.5}^{+.5} C(x) (x-F)^2 dx / C. \quad (19)$$

A more detailed description of the Pedersen-Prahm advection technique may be found in (16).

HEAT BUDGET FORMULATION

The primary emphasis of this application of the Laevastu thermal model is on heat budget rather than response of atmospheric parameters to ocean surface temperature under the gradient wind, which has been discussed by Laevastu, et al., (17), (18). A more detailed treatment of the heat budget components, including some terms not considered below, may be found in Laevastu (19). Young (20) provides quantitative values of the various heat budget terms for the southern California shelf area, which have been used as representative input for thermal effects.

Oceanic Heat Budget

A statement of the oceanic heat budget which is sufficient for the purposes of this study follows:

$$Q = Q_s - Q_r - Q_b - Q_h - Q_e + Q_m, \quad (20)$$

where:

Q	--net heat flux,
Q _s	--total incident (short wave) radiative heat flux,
Q _r	--reflected (short wave) radiative heat flux,
Q _b	--net atmospheric-oceanic (long wave) radiative heat flux,
Q _h	--sensible heat loss to (gain from) atmosphere (convective transfer or conduction),
Q _e	--evaporative heat loss (latent heat uptake by atmosphere),
Q _m	--heat induced by human efforts.

The preceding formulation ignores the following heat exchange processes: transfers through ocean bottom, kinetic transformation (tidal and wind friction), natural chemical processes, precipitation, fresh water runoff and net circulation through region boundaries. Man-induced heat exchange processes including power plant cooling, sewage and industrial outfalls, man-induced chemical processes, etc., may be handled as pollutant sources.

Heat Budget Components

Each of the natural components of Q is presented in cal cm⁻² day⁻¹ units (1 calorie = 4.18605 joules). The formulae of this section are presented essentially following Laevastu (19). Total daily insolation is given by:

$$Q_s = Q_{os}(1 - .0006c^3), \quad (21)$$

where c is the cloudiness in tenths of the sky and Q_{os} is the clear sky cloudless short wave radiation. Daily values of Q_{os} may be computed empirically as:

$$Q_{os} = .014A_n t_d, \quad (22)$$

where A_n is the noon altitude of the sun (degrees) and t_d is the length of the day (sunrise to sunset) in minutes. Shorter term computations modeling the day/night cycle would require a more definitive method, such as:

$$Q_{os} = 2736 \cdot \sin \bar{\alpha} \quad (23)$$

where $\bar{\alpha}$ is the mean altitude of the sun for the time period of interest.

The daily reflected radiation may be expressed in terms of Q_s in a linear relationship by:

$$Q_r = .087Q_s. \quad (24)$$

Although presented for daily values, Equation 24 could be used with Equations 21 and 23 for a first guess approximation of short term values.

Effective back radiation, the net long wave radiation of the atmospheric-oceanic system is computed as follows:

$$Q_b = (297.-1.86T_w-.95U_0)(1-.0765c) \quad (25)$$

where T_w is the water temperature, U_0 is the relative humidity and c , as before, is the cloudiness factor. Both the net atmospheric long wave radiation and the net back radiation from the ocean follow a fourth power law of their respective temperatures. Equation 25 is interesting since it combines both these long wave radiation terms into a single equation basically dependent on the water temperature alone. See Laevastu (19) for a description of Equation 25 development.

The evaporative heat loss (or gain) is computed as follows:

$$Q_e = 53.9(.26+.077W)(T_w-T_a) \quad (26)$$

where W is the wind speed in m/sec and T_a is the air temperature. A similar formulation is employed for the sensible heat loss (gain):

$$Q_h = 39.0(.26+.077W)(.98E_w-E_a) \quad (27)$$

where E_w is the saturated water vapor pressure of air at the temperature of the water surface and E_a is the water vapor pressure of air over the surface.

The man-induced component is determined externally based on the situation to be modeled.

MONTE CARLO SIMULATION

Monte Carlo techniques as a class simulate stochastic processes through the judicious application of a random number generator. The stochastic character of diffusive processes lends itself to simulation by Monte Carlo methods. In order to introduce the random element, the total velocity for a particular fluid particle is assumed to be composed of a mean flow velocity component and a turbulent flux velocity component. The HN model provides the mean flow velocity and the Monte Carlo scheme provides the turbulent flux velocity. Dispersion is thus modeled by simulating the diffusion process stochastically within the background fluid in motion. For a particular case, a sample of tracer particles representing the output of a source is tracked in time. The number of particles in the sample is determined by the particular case and the desired degree of statistical resolution.

Meier-Reimer (21) presented the results of several alternative approaches to applying Monte Carlo simulation to the diffusion problem and found the Monte Carlo method superior to either Lagrangian or Eulerian difference methods in terms of results as well as cost. Using a meteorological application Thompson (22) showed the Monte Carlo process to be simple and direct with a good match between statistically expected and numerically

experimental values for simple Fickian cases. Thompson also demonstrated the ease with which the method could be generalized to more complex dependency regimes and more sophisticated parametric representations.

SECTION 4

EXPERIMENTAL EXTENSIONS OF THE HN MODEL

THE NON-LINEAR ENHANCEMENT

Most of the Hansen type HN models have neglected the convective (advective) terms since analysis indicated that these non-linear terms were not significant for most practical applications. Further, retention of these terms to cover the general case was not economically justifiable and complicated the boundary problem. These non-linear terms are first order differential terms which should be analytically expected to show significant effects in fine mesh applications, especially where lateral flow specification is required, e.g., river inflow. The incorporation of the convective terms into the momentum equations was the first task in this effort to enhance the HN model for the study of near-shore processes.

Non-Linear Difference Form

Fractional z notation--

To simplify the description of the derivation of the difference form of the convective terms, a decimal fractional z notation, illustrated in Figure 9, has been used. All points in the staggered grid have been identified by fractional index values that have a common z grid origin. The staggered grid point $u(1,1)$ is represented as $u(1,1.5)$ and staggered $v(1,1)$ becomes $v(1.5,1)$. Thus fractional z notation is a positionally correct notation providing the flexibility to represent variables at any desired location.

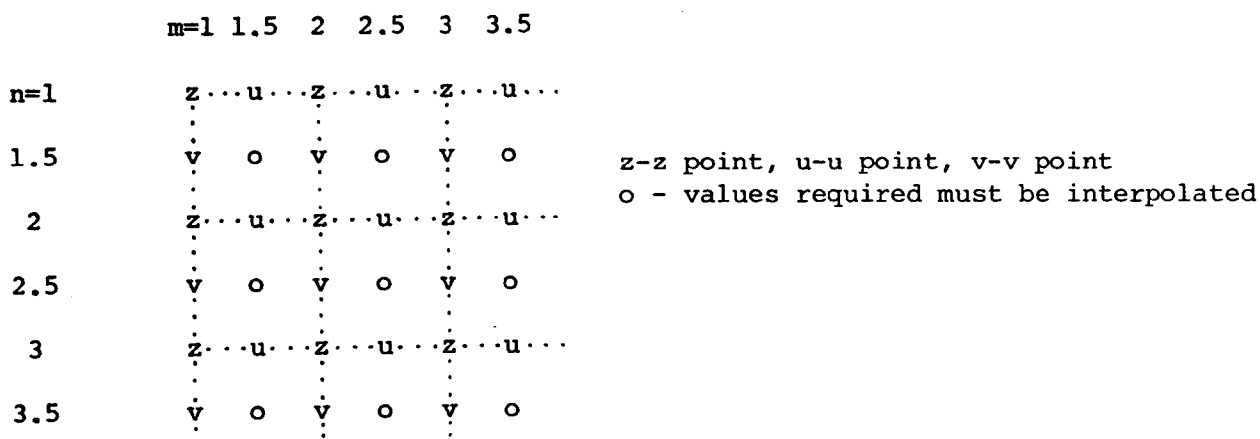


Figure 9. Fractional z index notation.

Derivation of the Difference Form--

The convective difference forms presented in Equations 5 and 6 are derived. Boundary conditions are treated separately. This derivation treats only those points not immediately adjacent to boundary points. Using fractional z notation Equation 2 is solved at $U(n,m+.5)$, and Equation 3 is solved at $v(n+.5,m)$. The convective terms from Equations 2 and 3 have been included here for convenience:

$$\begin{aligned} & \dots + U_i(U_i)x + V_i(U_i)y \dots, \\ & \dots + U_i(V_i)x + V_i(V_i)y \dots \end{aligned} \quad (28)$$

The difference form of Equations 28 was derived by replacing the partial differentials with spatially centered differences as follows:

$$\begin{aligned} (U_i)_x(n,m+.5) & \approx [U_i(n,m+1.) - U_i(n,m)]/2\ell, \\ (U_i)_y(n,m+.5) & \approx [U_i(n-.5,m+.5) - U_i(n+.5,m+.5)]/2\ell, \\ (V_i)_x(n+.5,m) & \approx [V_i(n+.5,m+.5) - V_i(n+.5,m-.5)]/2\ell, \\ (V_i)_y(n+.5,m) & \approx [V_i(n,m) - V_i(n+1.,m)]/2\ell. \end{aligned} \quad (29)$$

Equations 29 constitute difference approximations of the respective differential factors to first order accuracy; however, u and v velocity components are required at "z" and "o" points, as identified in Figure 9. As U and V values will not be available at "z" and "o" points, linear interpolation between available u and v points yielded:

$$\begin{aligned} (U_i)_x(n,m+.5) & \rightarrow [U_i(n,m+1.5) - U_i(n,m-.5)]/4\ell, \\ (U_i)_y(n,m+.5) & \rightarrow [U_i(n-1.,m+.5) - U_i(n+1.,m+.5)]/4\ell, \\ (V_i)_x(n+.5,m) & \rightarrow [V_i(n+.5,m+1.) - V_i(n+.5,m-1.)]/4\ell, \\ (V_i)_y(n+.5,m) & \rightarrow [V_i(n-.5,m) - V_i(n+1.5,m)]/4\ell. \end{aligned} \quad (30)$$

Returning to staggered grid notation resulted in the following difference approximations:

$$\begin{aligned} (U_i)_x(I) & \rightarrow [U_i(MP) - U_i(MM)]/4\ell, \\ (U_i)_y(I) & \rightarrow [U_i(NM) - U_i(NP)]/4\ell, \\ (V_i)_x(I) & \rightarrow [V_i(MP) - V_i(MM)]/4\ell, \\ (V_i)_y(I) & \rightarrow [V_i(NM) - V_i(NP)]/4\ell. \end{aligned} \quad (31)$$

Equations 31 constitute difference approximations of the respective differential factors to second order accuracy.

Substituting the Equations 31 into Equations 29, as required, transposing terms to the right-hand side of the equation and multiplying each equation by a factor of 2τ , yielded the difference forms presented in Equations

5 and 6 as follows:

$$\begin{aligned} & \dots - .5(\tau/\ell) \{ U_i(I) [U_i(MP) - U_i(MM)] + \overset{*}{V}_i(I) [U_i(NM) - U_i(NP)] \} \dots, \\ & \dots - .5(\tau/\ell) \{ \overset{*}{U}_i(I) [V_i(MP) - V_i(MM)] + V_i(I) [V_i(NM) - V_i(NP)] \} \dots \end{aligned} \quad (32)$$

where the star terms, $\overset{*}{V}$ and $\overset{*}{U}$, respectively, represent the linearly interpolated v velocity component at the u point, and the linearly interpolated u velocity component at the v point. (Note that $V_i(n, m+.5)$ and $U_i(n+.5, m)$ are not directly available in the difference scheme.)

Non-Linear Boundary Conditions

The boundary conditions, Equations 13 and 16, are effected by index substitution and would be the default convective computational boundary conditions (unless special measures were taken) due to the procedure of computing the convective terms. Equation 11 is also a default condition, but is considered to be correctly so (Figure 10). When index substitution occurs to effect conditions 3 and 6, the separation of the values differenced decreases by half due to the index modification, but the form of the difference computation causes division by the second order difference width (4ℓ). Linear extrapolation of the internal gradient would then easily be accomplished by a factor of 2. Leendertse (10) found that the two step implicit scheme showed characteristics of local instability when a linear extrapolation condition (zero friction) was applied at boundaries normal to the direction of flow. He had previously shown a theoretical tendency in this regard for a simplified equation set.

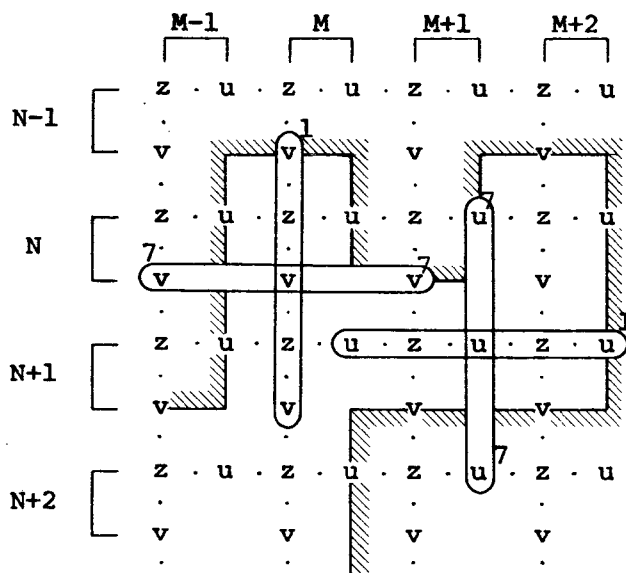


Figure 10. U, V non-linear computational stencils at closed boundaries.

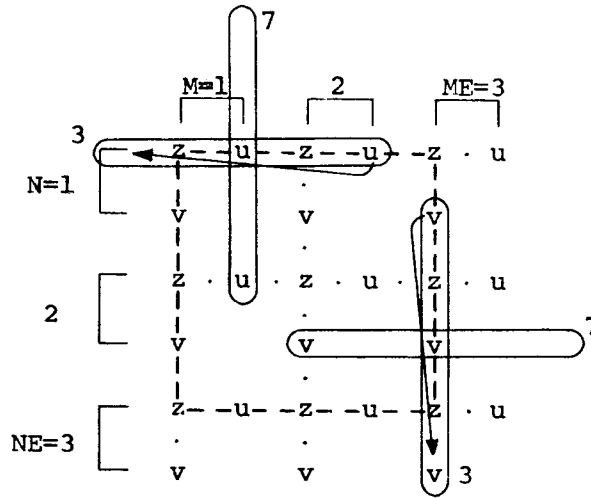


Figure 11. U, V non-linear computational stencils at open boundaries.

Instability with respect to the slightly stronger (friction $\neq 0$) condition, Equation 13, was found when the convective terms were applied to a Prudhoe Bay model by EPA at Corvallis. Subsequent experiments with the Prudhoe Bay model showed that when the first order form of Equation 13 was replaced with the second order form of the same condition (precisely twice the implied friction of the first order form) that the instability disappeared (see Figure 11). This is the same result that Leendertse (10) found successful. The source of the initial instability in the Prudhoe Bay model was apparently local, which, as Leendertse indicated, was fed back into the equations through the non-linear terms to drive the entire area to instability.

No apparent instability was introduced when the first order tangential condition, Equation 16, was modified to a second order zero friction (free slip) condition by extrapolation of the internal gradient. Equation 33 defines the free slip Neuman condition used for the non-linear terms at all boundaries tangential to flow in lieu of Equation 16.

$$\text{Condition 7: } \partial [\tilde{v}(x,y) \cdot \tilde{T}] / \partial N \Big|_{\Gamma} = \lim_{s \rightarrow 0} \partial [\tilde{v}(x+\epsilon s, y+\delta s) \cdot \tilde{T}] / \partial N. \quad (33)$$

The parameters ϵ and δ are chosen as 0, ± 1 , irrespectively, so that a boundary point (x,y) is approached from seaward along N as s approaches 0. The sign of the non-zero parameter would reflect the appropriate direction.

Figures 10 and 11 depict computational stencils enclosing geographic positions for values required for the non-linear term computations. Superscript numerals in these figures identify the numbered boundary conditions specified in Equations 11-16 and 33 that are applied. Figure 10 should be interpreted that the condition is applied at land edges rather than across narrow channels. The cross channel component of the non-linear term is zero for a single cell channel. Arrows, where shown in these figures,

indicate effective value transfer used to impose the boundary conditions. TABLE 1 provides a comparative description of the various conditions.

An item of further study should be the use of this free slip boundary condition for other than convective term computations at tangential open boundaries as a means of avoiding even the slight lateral friction currently imposed by Equation 16.

THE LAYER DISAPPEARANCE ENHANCEMENT

Many regions in the coastal zone are characterized by the cyclic emergence and inundation of extensive mud flat or marshy areas due to shallow bathymetry and tidal range. The optimized HN model assumed fixed land-sea boundaries based on initial depth fields. The boundary conditions associated with those fixed boundaries were violated when tidal flat conditions occurred. The second task proposed to modify the HN model to handle variable land-sea boundaries and their associated boundary conditions. To simulate tidal flat regions the effective land-sea boundaries were made a function of layer thickness. The variable land-sea boundary capability was designed to be an optional, rather than an integral feature to have minimal effect on the basic model. An hypothetical tidal flat bathymetry was designed to facilitate procedural verification testing which would thoroughly exercise the dynamic boundary operation. Additional verification tests were performed on the grid representing Prudhoe Bay, Alaska, which had been prepared by EPA at Corvallis.

Layer Disappearance Procedures

Figure 12 depicts the (n,m) cell which is defined with the $z(n,m)=z(I)$ point in the top center of the cell with vertical boundaries passing through the $u(I)$ point to the east, the $u(MM)$ point to the west, the $v(NM)$ point to the north and the $v(I)$ point to the south, and horizontal boundaries at the upper and lower surfaces of the layer. When fluid volumes are excluded or included in the computation they comprise a single cell or group of such cells.

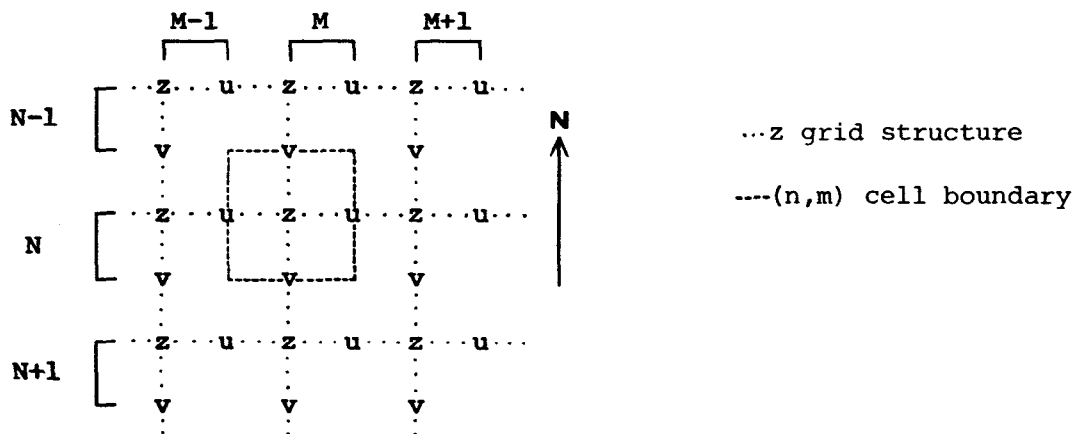


Figure 12. The (n,m) cell.

Cell Closure Procedure--

Following the normal computation of layer surface deviation (ζ) and thickness (H_u, H_v), the average cell thickness, \bar{H} , is computed at the z point and compared to a prescribed minimum thickness, H_{min} . If $\bar{H} \leq H_{min}$, the cell should have been considered closed during the computation of ζ , H_u and H_v . A closure status is maintained for each cell and this is changed to indicate full closure. For each cell so indicated, those associated velocity components not bordering on a land cell are reset to zero, and the status of adjacent, non-land, open cells is modified to show partial closure.

If $\bar{H} > H_{min}$, it is possible that some thicknesses associated with this cell may individually be less than or equal to H_{min} . For this case, a partial closure of the cell is effected by setting the associated velocity component to zero and maintaining the closure status appropriately.

Re-evaluation of Layer Surface Deviation--

The velocity components as computed in the last computational step may have been modified by cell closure procedures. The layer surface deviations (ζ) logically adjacent to the modified components must now be recomputed based on the effectively modified land-sea boundary. The most compelling reasons to perform the recomputation are: 1) to maintain the land-sea boundary conditions described for regular land-sea boundaries; and 2) to maintain the layer surface deviations associated with fully closed cells consistent with respect to surrounding layers. Based on the cell closure status, actions to be effected in the single layer case follow:

- 1) open: no action;
- 2) partial closure: recomputation of $\zeta^{t+\tau}$;
- 3) full closure: reset $\zeta^{t+\tau}$ to the value of $\zeta^{t-\tau}$.

In the multi-layer case the same closure status conditions are possible independently in each layer. The nature of the continuity equation, however, is such that a lower layer may have an effect on an upper layer, notwithstanding the upper layer's closure status. In the recomputation procedure, if a lower layer ζ_i requires:

- 1) recomputation (partial closure);
- 2) non-zero "adjustment" (from the $i+1$ layer);
- 3) resetting of $\zeta_i^{t+\tau}$ to the value of $\zeta_i^{t-\tau}$ (full closure);
- 4) a combination of 1) and 2); or
- 5) a combination of 2) and 3);

then ζ_{i-1} ($i-1 \neq 0$) requires an adjustment Z'_i . The adjustment of Z'_i is equal to the recomputed or reset and/or adjusted $\zeta_i^{t+\tau}$ less the value of $\zeta_i^{t-\tau}$. Thus the recomputation procedures must occur in precisely the same order that the original ζ computations took place, i.e., lower layer ζ_i terms are computed first so that the Z'_i may be computed for use in succeeding layer computation. Based on cell closure status, actions to be effected in the multi-layer case

follow:

- 1) open: $\zeta_i^{t+\tau} = \zeta_i^{t+\tau} + Z'_{i+1}$;
- 2) partial closure: $\zeta_i^{t+\tau} = \zeta_i^{t+\tau}(\text{recomp}) + Z'_{i+1}$;
- 3) full closure: $\zeta_i^{t+\tau} = \zeta_i^{t-\tau} + Z'_{i+1}$.

Boundary Condition Consideration

Velocity components which have been set to zero by the cell closure procedures are treated as if they were a true land-sea (closed) boundary by the recomputation of ζ as it occurs. Second order computations in ζ ($\bar{\zeta}$) are discontinuous since $\bar{\zeta}$ is not included in the recomputation. (Figure 8 does not apply to recomputation). Further, recomputed (or changed) ζ values do not effect any changes in ζ values which are adjacent to the recomputed (or changed) ζ values. Tests calculating ζ with a correctly recomputed $\bar{\zeta}$ did not significantly alter or improve the results, ergo $\bar{\zeta}$ is not recomputed.

Second order computations in U and V (\bar{U} , \bar{V} and the convective computations) are also discontinuous, but only for the step in which a particular cell side is first closed (set to zero.) These second order U and V computations adjacent to a cell side (for which it is determined for the first time that the velocity component should have been zero valued) were computed using a value other than zero. All such succeeding second order computations adjacent to continuously closed cell sides are computed correctly for all subsequent steps including the step in which the side is reopened. These second order discontinuities in the various computations have not and should not provide any problems, since the smoothing through the remainder of the field in subsequent steps has been designed to remove such low order perturbations.

THERMAL ADVECTION EXTENSION

The advection of a thermal discharge is a common practical problem of interest in the coastal zone, particularly with respect to power plant cooling water and, to a lesser degree, waste water discharges. If one ignores the density effects of the heated fluid on the dynamics of a region, the HN computed current velocities for the top layer may be reasonably used to advect a thermal discharge through the region. The Pedersen-Prahm (16) advection scheme has been chosen since it is a conservative scheme without the pseudo-diffusion of Eulerian difference methods. In order to model the heat budget effects on the thermal discharge as it is transported by the currents through the region, the Laevastu thermal techniques (19) were selected.

A version of the Pedersen-Prahm advection routine developed by J. Harding of Naval Environmental Prediction Research Facility (NEPRF), Monterey, was combined with the thermal techniques used by Laevastu, et al., (17), (18). Both FORTRAN computer program systems required conversion to the Lawrence Berkeley Laboratory (LBL) CDC 7600 and required appropriate linkages to weld

the two systems into a single practical system of thermal advection. The current scope of the task does not admit the study of diffusive effects.

Thermal Equations

The change of temperature T of a volume C of water induced by the quantity of added heat K in addition to "ambient heat" is given by:

$$\Delta T = K / \bar{c} \rho C, \quad (34)$$

where \bar{c} is the average specific heat of the fluid and ρ is the density, assumed uniform through the layer. The quantity of heat introduced over an area A during a time period 2τ is provided by the heat budget formulation:

$$K = Q A 2\tau = (Q_s - Q_r - Q_b - Q_e - Q_h + Q_m) A 2\tau; \quad (35)$$

thus

$$\Delta T = (Q_s - Q_r - Q_b - Q_e - Q_h + Q_m) 2\tau / \bar{c} \rho d \quad (36)$$

where d is the depth of the heated fluid.

These equations assume that all added heat is absorbed, stored or lost in the upper thickness d of the surface layer. This depth of the heated fluid is a dynamic quantity which may be determined from the advected volume being followed and the distribution information maintained by the moment method of advection. The distribution information also allows computation of the average temperature of the entire cell.

Duplex Thermal Advection

The advection procedure requires a conservative quantity. The volume of the heated fluid is one obvious conservative quantity where the temperature is not conservative. Equation 34 shows that the volume is not sufficient to determine ΔT . Both the volume and the "added heat" must be known to determine the change in temperature. Since both quantities must be followed for a thermal procedure, the process is being called "duplex thermal advection." In the duplex procedure the full method of moments is applied to the volume of the heated fluid and only the zeroth moment values are computed for the "added heat." The first and second moment information computed for the volume is assumed to hold for the "added heat" as well.

The time step required to maintain stability in the method of moments is determined by the velocity of the fluid rather than the Courant-Friedrich-Lewy criterion as in the HN model. To take advantage of the longer time step permitted, the duplex thermal advection has been developed as a separate program. This also makes it possible to perform a series of numerical experiments based on a single set of HN velocity fields.

The duplex method is composed of a sequence of procedures performed at each time step. The operations include thermal and advective processes, each of which is computed independently. The advective process assumes the thermal process is fixed in time and the thermal process assumes that the advective process is fixed in time for the computational interval.

Subscripts refer to thermal processes: superscripts refer to advective processes. (If a sub- or superscript is missing, it is of the same time

order as the sub- or superscript that is present.) The sequence of procedures follows:

1. $t=t_0$, continue at procedure #7; (initialization)
2. $(Tw_{t+2\tau}^t, Ta_{t+2\tau}^t, Aw_{t+2\tau}^t) = \text{thermal } (Tw_t, Ta_t, Aw_t)$; (thermal step)
3. $T_{t+2\tau}^t = (Tw_{t+2\tau}^t - Aw_{t+2\tau}^t) / (RxRy)$; (inverse interpolation)
4. $K_{t+2\tau}^t = \rho c C^t \Delta T_{t+2\tau}^t$; (added heat computation)
5. $(C_{t+2\tau}^{t+2\tau}, K_{t+2\tau}^{t+2\tau}) = \text{advect}(C^t, K_{t+2\tau}^t) (U, V)^t$; (advection step)
 $(RxRy \text{ becomes } Rx_{t+2\tau}^{t+2\tau}, Ry_{t+2\tau}^{t+2\tau})$
6. $t=t+2\tau$; (full step accomplished)
7. $C_t^t = C^t + \Delta C^t$, (also adjust $RxRy$); (pollution volume increment)
8. $K_t = K_t + \Delta K_t$; (pollution heat increment)
9. $\Delta T_t = K_t / (\rho c C^t)$; (temperature change computation)
10. $Tw_t = T_{t+2\tau}^t RxRy + Aw_t$; (cell temperature interpolation)
11. when $t=t_e$ stop, otherwise continue at procedure #2;

where:

Rx, Ry	--horizontal width factors in grid step units related to second moment of pollutant in cell (Equation 17),
Ta	--air temperature,
t_e	--end time,
t_0	--start time,
Tw	--surface water temperature,
ΔT	--temperature in excess of ambient for the heat polluted volume,
Aw	--ambient water temperature,
thermal	--thermal procedure
advect	--duplex advective procedure.

The device of starting at procedure 7 prevents advection or thermal adjustment from being applied to heated material added in the same step. Procedures 7 and 8 are determined externally by the case of interest. Note that the width factors maintained by the advective procedure must be initialized or adjusted in procedure 7. Procedure 9 computes the temperature anomaly (or temperature in excess of ambient temperature) for the volume associated with the excess heat. Procedure 10 interpolates from the temperature anomaly obtaining the horizontal mean temperature for each cell. Procedure 11 terminates the computation at the appropriate point or returns to procedure 2.

The ambient temperature is maintained constant for the experiments presented in the next section. Equation 23, however, provides the key to modeling a diurnal cycle.

MONTE CARLO EXTENSION

Practical diffusion problems occur more frequently than anyone would like. Controlled and uncontrolled petrochemical, chemical and sewage spills are particularly of interest in coastal areas due to the potential ecological effects, property damage and human environmental factors. The HN model provides the detailed velocity information required to give a solution to the basic vector path problem of following a particular spill. It has been shown by Maier-Reimer (21) that when a Monte Carlo technique is appropriately applied to the basic HN velocity components associated with a particular conservative element of the spill, one may expect to model the diffusive process much more reasonably than with other ostensibly more explicit procedures. Pure Eulerian difference schemes generally produce an extremely unrealistic level of artificial diffusion generally associated with the interpolation inherent in these schemes. Pure Lagrangian schemes break down due to Lagrangian grid distortion after an unreasonably short time. The Monte Carlo scheme is pseudo-Lagrangian in that specific pollutant particles are followed in time, but the Eulerian framework is maintained to provide the velocities for each Lagrangian step. Each marker particle is advanced one Lagrangian step by application of a mean flow velocity interpolated to the present position of the particle from the Eulerian grid values. The final location of the marker particle at the end of the step is further determined by the application of a random velocity increment consistent with the statistical view of diffusion. The u and v components of the velocity increment are selected independently by a stochastic process. The stochastic process is constrained to provide each selected component within a discrete range determined by the diffusion process and the time step between available Eulerian velocities.

The Procedure

A Monte Carlo procedure may be defined for a set of Lagrangian tracer particles in horizontal coordinates as follows:

$$\begin{aligned}x_j^{t+2\tau} &= x_j^t + (U_j^{t+2\tau} + u_j^{t+2\tau}[P]) \cdot 2\tau, \\y_j^{t+2\tau} &= y_j^t + (V_j^{t+2\tau} + v_j^{t+2\tau}[P]) \cdot 2\tau,\end{aligned}$$

for j th particle, where the x, y are position vector components, the U, V are mean flow velocity components, and $u[P], v[P]$ are variates stochastically selected from P , the total population of possible turbulent flux velocity components. In actual computations the tracer particles are followed in dimensionless grid coordinate (n, m) units as:

$$\begin{aligned}m_j^{t+2\tau} &= m_j^t + (U_j^{t+2\tau} + u_j^{t+2\tau}[P]) \cdot \ell, \\n_j^{t+2\tau} &= n_j^t - (V_j^{t+2\tau} + v_j^{t+2\tau}[P]) \cdot \ell,\end{aligned}$$

where the $U[P], V[P]$ are selected from P independently in order to describe a constant diffusion coefficient.

The Stochastic Process

The particular stochastic process employed in this Monte Carlo scheme is defined as follows:

$$p_j = S(R_j - .5),$$

where p_j is the j th random variate "selected" from P , S is the stochastic coefficient and R_j is a pseudo-random number evenly distributed between 0 and 1. Successive independent selection of the x and y components results in an even distribution of the resultant turbulent flux velocity in a square of side S centered at the tip of the mean flow velocity vector. According to Meier-Reimer (21), the resulting distribution of tracer particles is statistically isotropic after two time steps and Gaussian after about eight time steps. Choosing $S=1.0$ results in a maximum effective "diffusion velocity" of the order of .5 cm/sec. Meier-Reimer (21) indicated that a diffusion velocity of the order of .5 cm/sec should be appropriate for most seas and oceans. Some adjustment of the stochastic coefficient may be necessary to achieve an average "diffusion velocity" of .5 cm/sec or some other characteristic velocity. Both Meier-Reimer (21) and Thompson (22) have presented some work with cases where the diffusion coefficient was allowed to vary in time and space. Extension of the present work to such cases should present no serious difficulties.

SECTION 5

RESULTS AND DISCUSSION

This section presents the results of the various extensions and enhancements through exposition of several figures. The figures present selected results for a hypothetical area designed to verify the procedures implemented. Literally thousands of figures, interesting in their own right, could have been prepared from the computational data; however, a few representative figures were deemed sufficient to present the case for the procedures.

NON-LINEAR TERM ENHANCEMENT

A special coastal grid with depth profile depicted by Figure 13 was designed to verify the procedures introduced to implement the non-linear terms. The 20X30 grid was characterized by longshore uniformity. The "optional" island indicated in Figure 13 was the only break in the uniform offshore depth profile when present in column 13 of the z grid. A combination of factors including depths surrounding the island, the longshore uniformity and the grid length selected (1.5 Km) resulted in essentially no significant differences between linear and non-linear cases of like bathymetry over a tidal period.

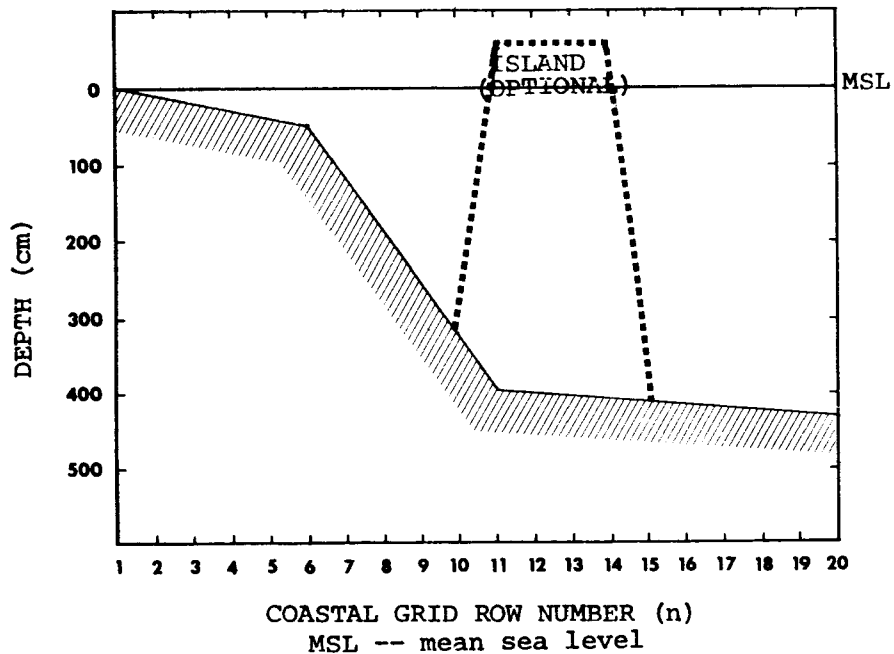


Figure 13. h_u depth profile for coastal grid.

The grid developed to verify procedurally the tidal flat enhancement was selected to verify the non-linear enhancement. Figures 14 and 15 present the tidal flat grid and associated bathymetry. TABLE 2 provides detailed grid and run specifications for the typical computer model run involving the tidal flat grid.

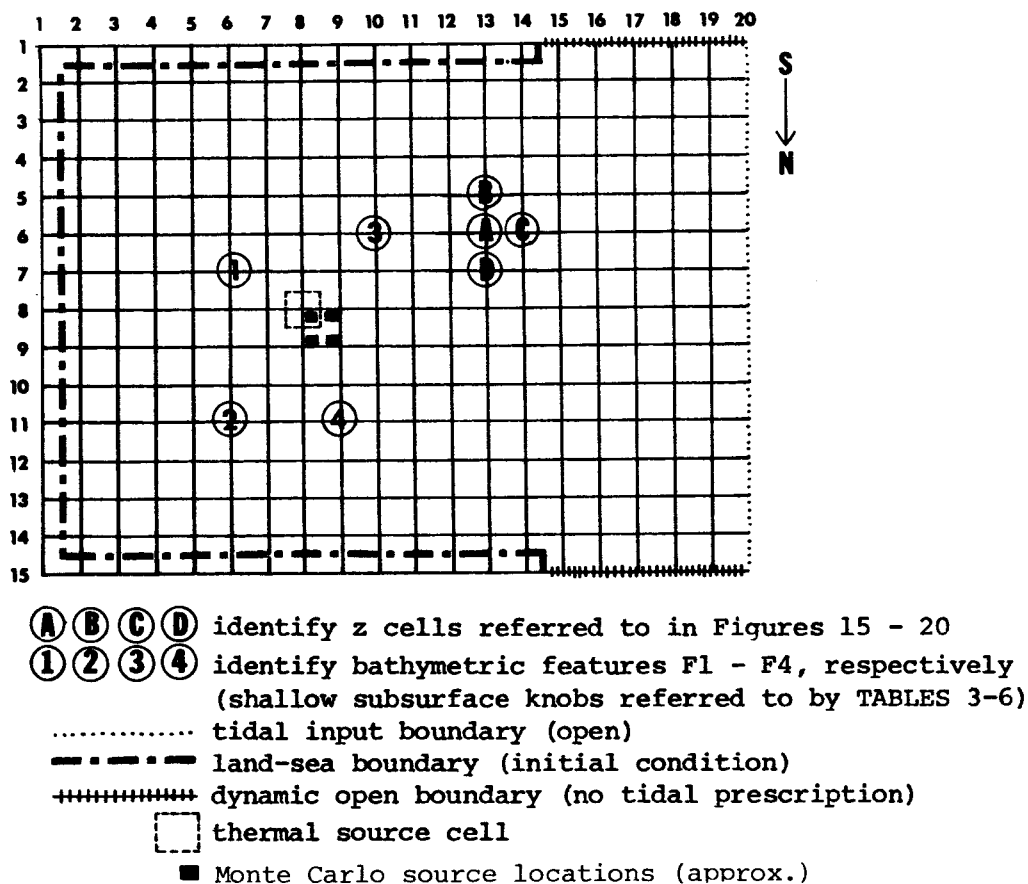


Figure 14. Tidal flat grid.

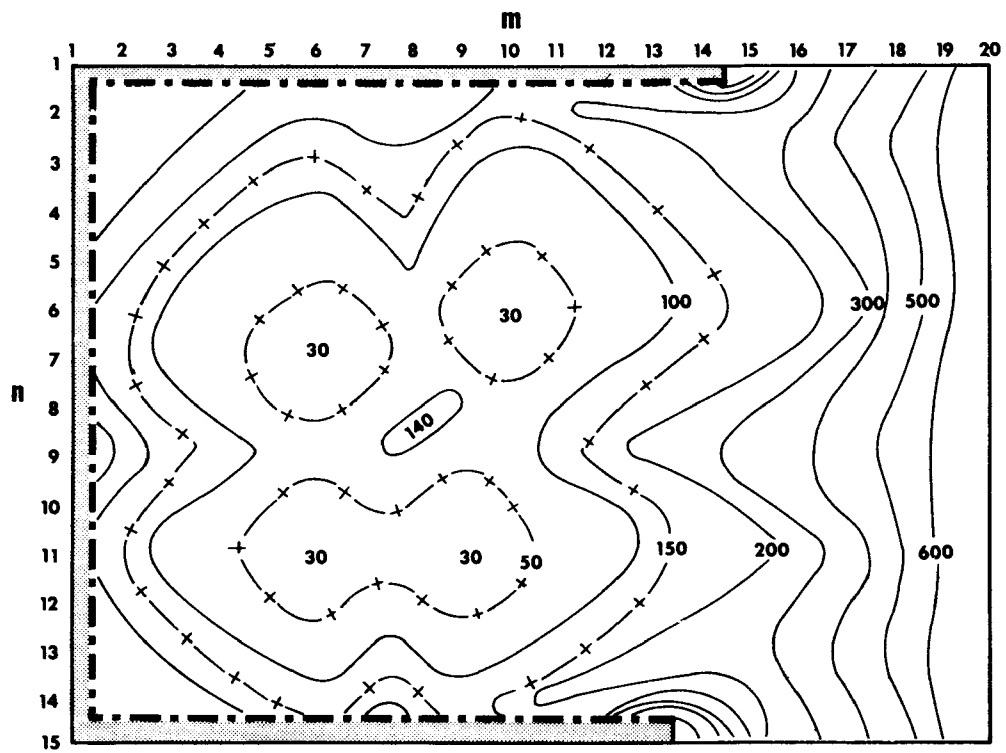


Figure 15. Tidal flat grid bathymetry (depths in cm).

TABLE 2. TYPICAL TIDAL FLAT GRID AND RUN SPECIFICATIONS

DATA CARD	PROGRAM VARIABLE	VARIABLE DESCRIPTION	VARIABLE VALUE ASSIGNMENT
NAME	IC1(2)-(9)	Grid description	EPA TIDAL FLAT TEST GRID
GRID	NE ME DL(2l) ROTANG ALAT R(r)	No. of Rows No. of Columns Grid length Rotation angle Average latitude Friction coefficient	15 20 1/3 Km 180° (implies (1,1) is the SE corner of grid) 45° (used to compute f and g) .003
LAYS	(k) HL(1) ALPHA(α) RHO(ρ) HMIN	No. of layers Maximum depth of layer Smoothing parameter Density Minimum allowable depth	1 660 cm .99 1.022 1.0
TIME	MODOUT ITO ITS(t_0) ITE ITINC(2 τ) IPO IPMOD	Data save step Data save start Start computation End computation Computational step Print step Print start	120 sec 120 sec (for runs saving data) 0 sec 31200 sec (8.67 hrs) 30 sec 1200 sec 1200 sec
FACT	TIDSPD(1)	Constituent speed	45°/hr (false "tide"-8 hr period)
TIDE*	ITIDE(1),(2) ITIDE(3),(4) ITIDE(5) ITIDE(1) ITIDE(5)	Min/max row spec. Min/max column spec. Tidal offset time Constituent phase shift Constituent amplitude	1,15 20 (western boundary specification) 0 sec 90° 130 cm
COMP	MODEL	Grid I.D. No.	998

*The open portions of the northern and southern boundaries were computed dynamically based on internal information and boundary conditions as specified previously.

TABLES 3-6 present linear and non-linear configuration development of the sometime tidal flat "islands" associated with bathymetric features F1 through F4 as identified in Figure 14. Configuration development in TABLES 3-6 is shown in full cell steps. The differences between the linear and non-linear computational modes is apparent. The non-linear model tends to "lead" the linear model with notable exceptions. The major exceptions relate to a change in the order of appearance of individual cells when the model is shifted into the non-linear mode. These variations in order and relative timing of appearance of individual cells in the development of both flats F3 and F4 imply a redistribution of the velocity field in the vicinity of these features.

In general the amplitude of the wave incident on the eastern closed bound (the back of the "bay") is less for the non-linear model than for the linear model. This is in agreement with an energy shift from longer to shorter wavelengths for the non-linear model.

LAYER DISAPPEARANCE ENHANCEMENT

A tidal flat grid and bathymetry were designed to verify thoroughly the procedures introduced in the layer disappearance enhancement of the HN model as shown in Figures 14 and 15. TABLE 2 provides detailed grid and run specifications for the typical computer model run involving the tidal flat grid. TABLES 3-6 present configuration development of the tidal flat segments associated with bathymetric features F1 through F4 as identified in Figure 14. All configuration development in TABLES 3-6 is presented in full cell steps. These tables were designed to show the differences between linear and non-linear model versions but quite adequately show the functional aspects of the layer disappearance modifications in those computational regimes.

For a more detailed view of a particular closure case, Figures 16 through 19 present a series of snapshots of actual configurations showing tidal flat development in cell side closure steps. These figures can be directly compared to the non-linear case configurations shown in TABLE 3.

Figure 16 presents an "initial" closure configuration with specific reference to cells A, B, C and D. Initially A is closed on the north and B, C and D are open. In Figure 17 the cells are shown at a subsequent time where A is closed to the north and east, D is closed to the south, and B and C are open. Figure 18 presents a later time showing A fully closed while B and D are each closed on a single side. Figure 19 presents a still later time where D becomes closed on two sides.

Figures 20 and 21 present HN computed time series data at time step intervals for ζ at A, B, C and D for separate periods. Tidal prescription from a tidal boundary point is also included for reference. Figure 20 brackets the snapshot times presented in Figures 16-19 showing the relative "sea height" for each of these cells through time compared to the tidal prescription. Note the gradual slope change in ζ_A down to the point of closure of cell A. A similar character is observed in the profile of ζ_D subsequent to the closure of the south side of cell D (Figure 17.) Neither the closure of a side of cell A, nor the full closure of cell A, introduced any evidence of instability locally in cell A or adjacent cells B, C and D.

TABLE 3: FLAT F3 FORMATION; NON-LINEAR VS LINEAR

FLAT CELL APPEARANCE ORDINAL	NON-LINEAR			LINEAR		
	(n,m) LOCATION	TIME	CONFIGURATION	(n,m) LOCATION	TIME	CONFIGURATION
1	(6,11)	16980	O+	(6,11)	17040	O+
2	(6,12)	17280	O++	(6,12)	17430	O++
3	(7,11)	17730	O ₊ +	(7,11)	17760	O ₊ +
4	(5,11)	17760	O ₊ +	(5,11)	17940	O ₊ +
5	(6,10)	18210	⊕ ₊ +	(6,10)	18030	⊕ ₊ +
6	(6,13)	18240	⊕ ₊ ++	(6,13)	18300	⊕ ₊ ++
7	(7,12)	18390	⊕ ₊ ++	(7,12)	18420	⊕ ₊ ++
8	(5,10)	18480	⊕ ₊ ++	(5,10)	18420	⊕ ₊ ++
9	(5,12)	18870	⊕ ₊ +++	(5,12)	19140	⊕ ₊ +++
10	(4,11)	19050	⊕ ₊ +++	(8,11)	19260*	⊕ ₊ +++
11	(8,11)	19320*	⊕ ₊ +++	(4,11)	19410	⊕ ₊ +++

* Connects to Flat F4 to form F34 at __.
 O Represents shallow knob at (6,10) at initial condition
 (Bathymetric feature F3, Figure 13.)

TABLE 4: FLAT F4 FORMATION; NON-LINEAR VS LINEAR

FLAT CELL APPEARANCE ORDINAL	NON-LINEAR			LINEAR		
	(n,m) LOCATION	TIME	CONFIGURATION	(n,m) LOCATION	TIME	CONFIGURATION
1	(11,10)	17100	O+	(11,10)	17130	O+
2	(11,11)	17340	O++	(11,11)	17400	O++
3	(12,10)	17640	O ₊ +	(12,10)	17760	O ₊ +
4	(10,10)	18060	O ₊ ₊	(10,10)	18060	O ₊ ₊
5	(11,12)	18180	O ₊ ₊ ₊	(11,9)	18120	⊕ ₊ ₊ ₊
6	(11,9)	18300	⊕ ₊ ₊ ₊	(11,12)	18210	⊕ ₊ ₊ ₊
7	(12,9)	18510	⊕ ₊ ₊ ₊	(12,9)	18340	⊕ ₊ ₊ ₊
8	(12,11)	18570	⊕ ₊ ₊ ₊	(10,11)	18660	⊕ ₊ ₊ ₊
9	(10,11)	18600	⊕ ₊ ₊ ₊	(12,11)	18720	⊕ ₊ ₊ ₊
10	(13,10)	18840	⊕ ₊ ₊ ₊	(13,10)	18990	⊕ ₊ ₊ ₊
11	(9,10)	19050	⊕ ₊ ₊ ₊	(9,10)	19020	⊕ ₊ ₊ ₊
	--	19320*	(no change) ⊕ ₊ ₊ ₊	--	19260*	(no change) ⊕ ₊ ₊ ₊

* Flat F3 connects to F4 by accretion to form Flat F34 at "--".
 O Represents shallow knob at (11,9) at initial condition
 (Bathymetric feature F4, Figure 13.)

TABLE 5: FLAT F1 FORMATION; NON-LINEAR VS LINEAR

FLAT CELL APPEARANCE ORDINAL	NON-LINEAR			LINEAR		
	(n,m) LOCATION	TIME	CONFIGURATION	(n,m) LOCATION	TIME	CONFIGURATION
1	(7,6)	18150	⊙	(7,6)	17970	⊙
2	(6,6)	19410	⊕	(6,6)	19110	⊕
3	(7,5)	19530	+⊕	(7,5)	19230	+⊕
4	(8,6)	20700	+⊕	(8,6)	20310	+⊕
5	(7,7)	20910	+⊕+	(7,7)	20520	+⊕+
6	(5,6)	21660	+⊕+	(5,6)	21120	+⊕+
7	(7,4)	21960	++⊕+	(7,4)	21390	++⊕+
8	(6,5)	22110	++⊕+	(6,5)	21510	++⊕+
9	(8,5)	22560	++⊕+	(8,5)	21990	++⊕+
10	--	25290*	++⊕+	(4,6)	25050*	++⊕+

* Flat F1 is connected to Flat F234 to form "U" shaped tidal flat F1234 at "--".

⊙ Represents shallow knob at (7,6) at initial condition (Bathymetric feature F1, Figure 13.)

TABLE 6: FLAT F2 FORMATION; NON-LINEAR VS LINEAR

FLAT CELL APPEARANCE ORDINAL	NON-LINEAR			LINEAR		
	(n,m) LOCATION	TIME	CONFIGURATION	(n,m) LOCATION	TIME	CONFIGURATION
1	(11,6)	18180	⊕	(11,6)	18000	⊕
2	(12,6)	19350	⊕ +	(12,6)	19050	⊕ +
3	(11,5)	19590	+⊕ +	(11,5)	19260	+⊕ +
4	(10,6)	20670	+⊕ +	(10,6)	20310	+⊕ +
5	(11,7)	20910	+⊕ +	(11,7)	20460	+⊕ +
6	(11,8)	20970*	+⊕ +	(11,8)	20550*	+⊕ +
7	(13,6)	21810	+⊕ +	(13,6)	21270	+⊕ +
8	(12,7)	21870	+⊕ +	(12,7)	21330	+⊕ +
9	(12,8)	21990	+⊕ +	(12,8)	21420	+⊕ +

* Flat F2 connects by accretion to Flat 34 to form lazy "L" shaped tidal flat F234 at "l".

○ Represents shallow knob at (11,6) at initial condition (Bathymetric feature F2, Figure 13.)

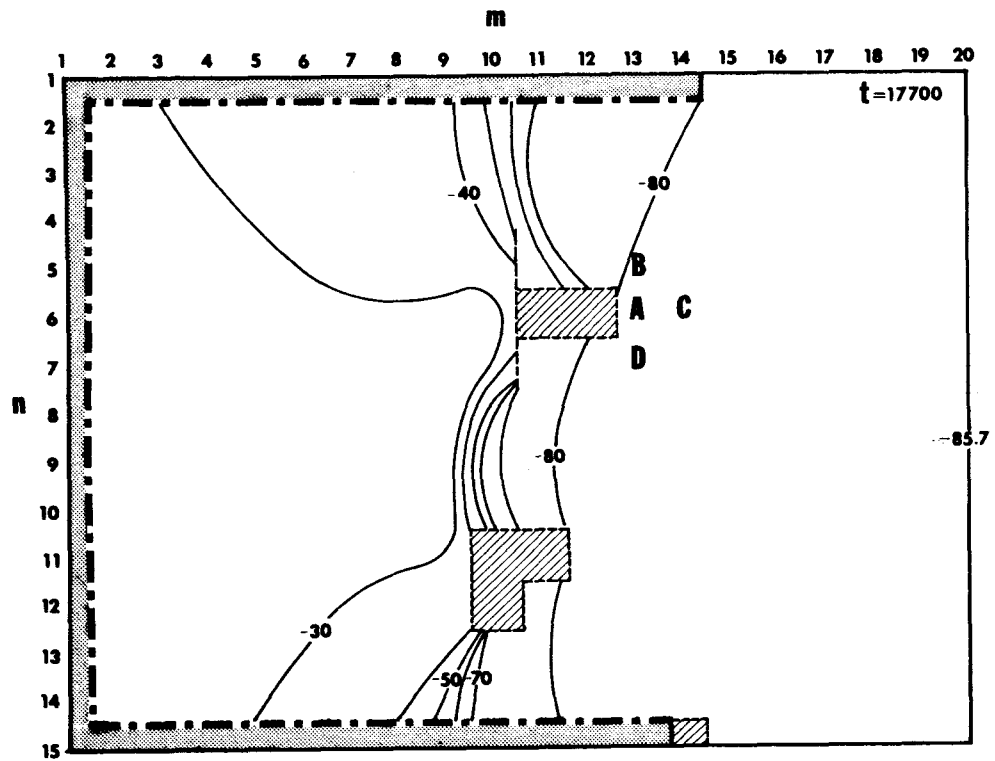


Figure 16. Closure configuration TFC: $t = 17700$ sec.

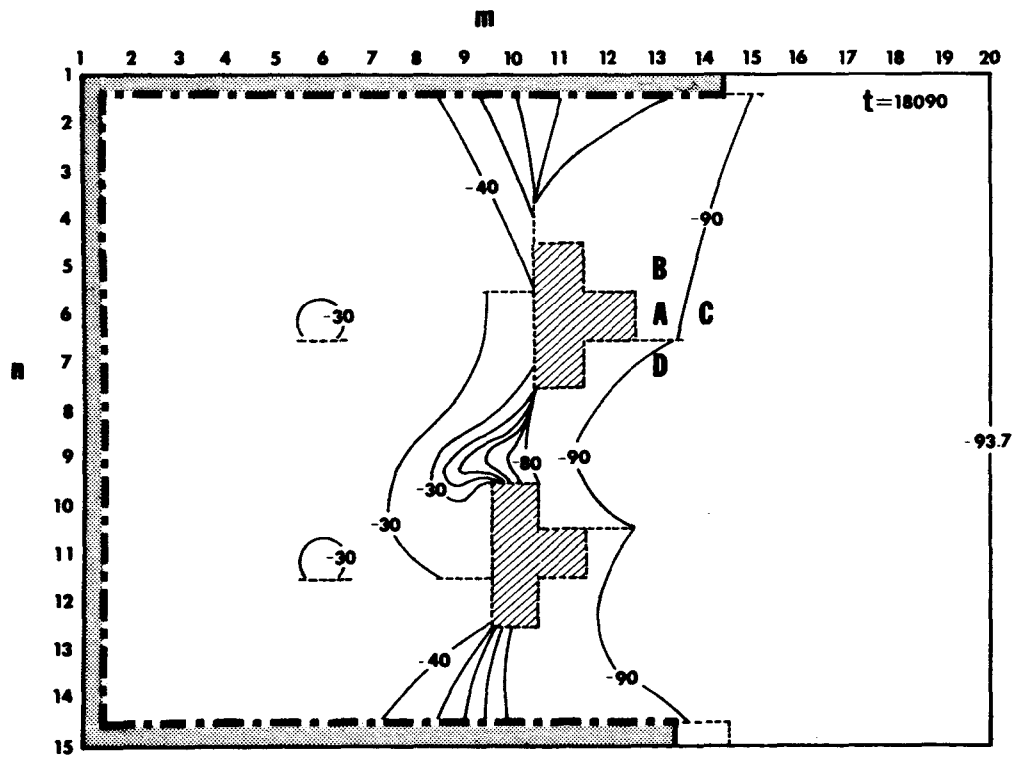


Figure 17. Closure configuration TFC: $t = 18090$ sec.

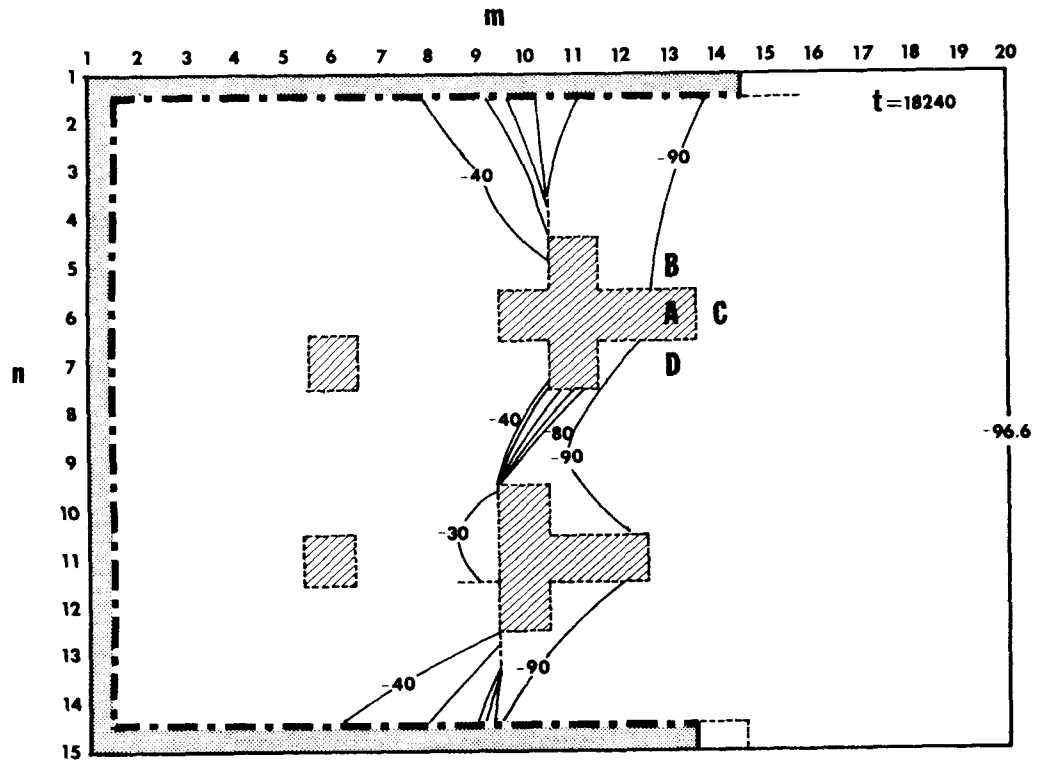


Figure 18. Closure configuration TFC: $t = 18240$ sec.

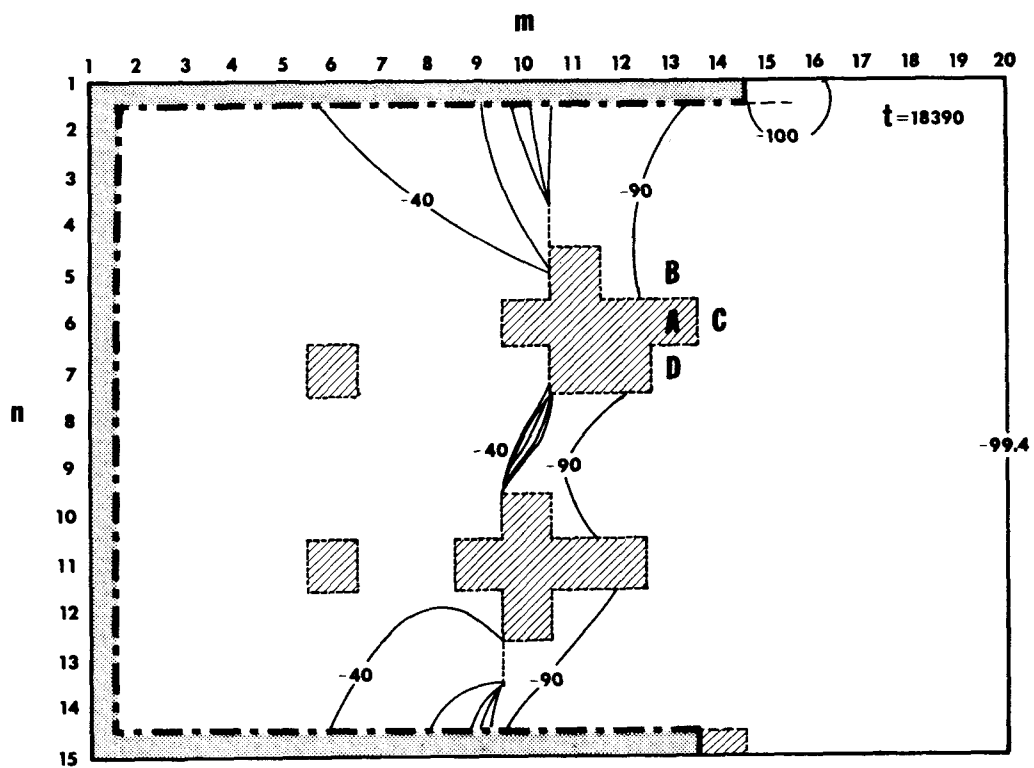


Figure 19. Closure configuration TFC: $t = 18390$ sec.

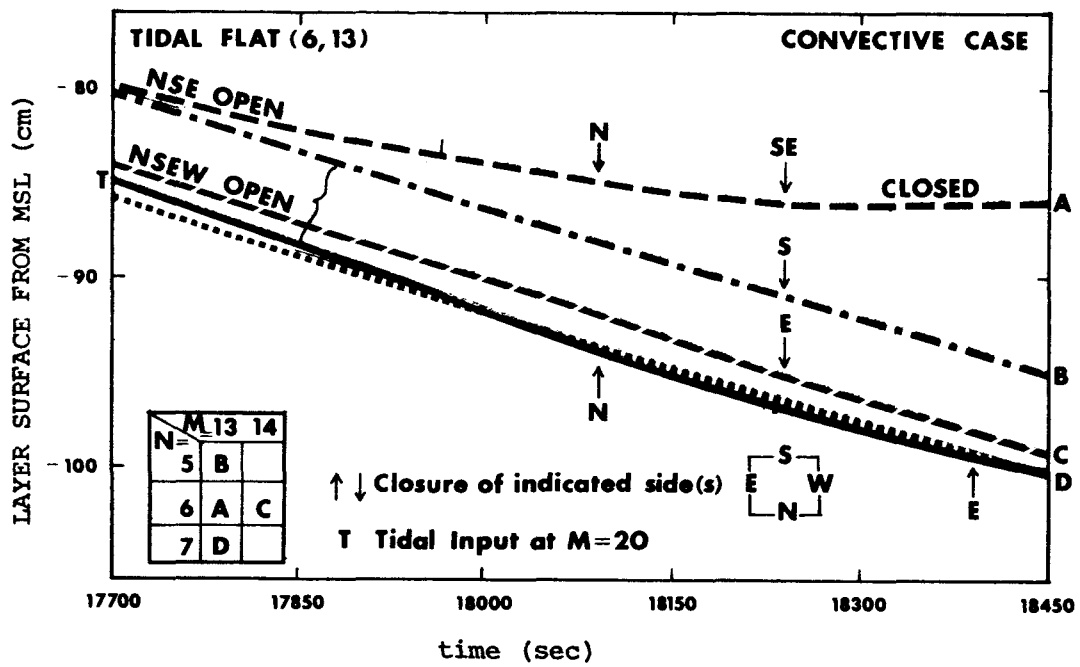


Figure 20. Closure analysis for TFC cell (6, 13).

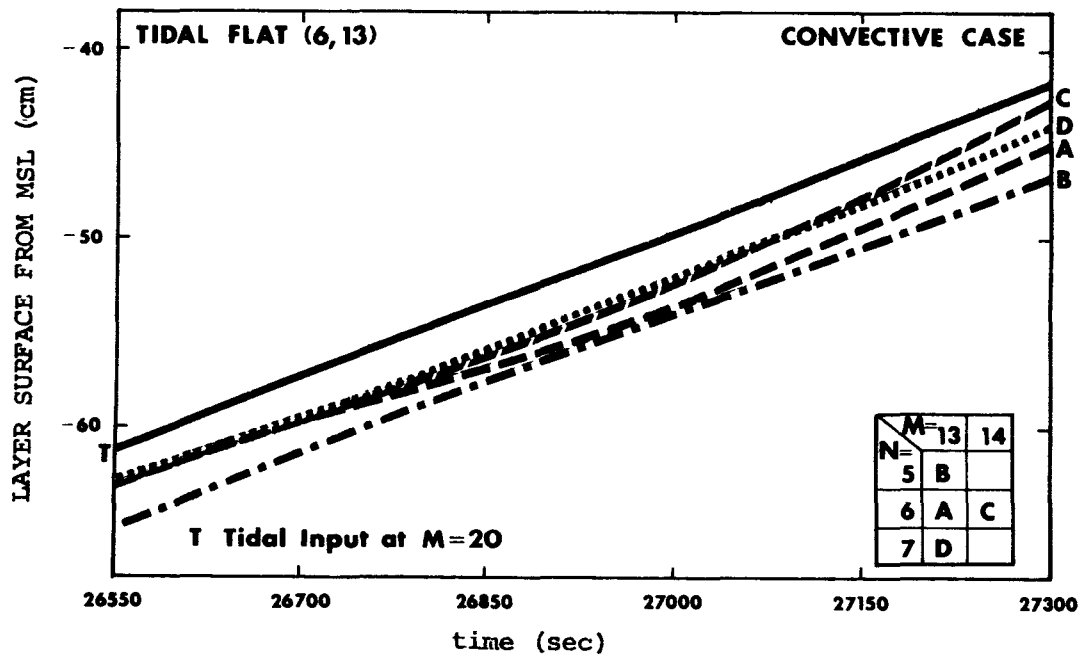


Figure 21. Post-reopening analysis for TFC cell (6, 13).

Figure 21 presents a much later period of time than Figure 20. Cells A, B, C and D had just been reopened by the initial time of Figure 21. Although waves of a period shorter than the "tidal cycle" are evident in the data, there is no indication of local instability at any of the reference points. Figure 22 depicts a relatively advanced stage of tidal flat development indicating maximum seaward advance of the tidal flat array. The connection of tidal flats F2, F3 and F4 have created a semi-enclosed tidal pool which drains to the south and east. Later a "U" shaped configuration, draining only to the east, develops in both the linear and non-linear modes.

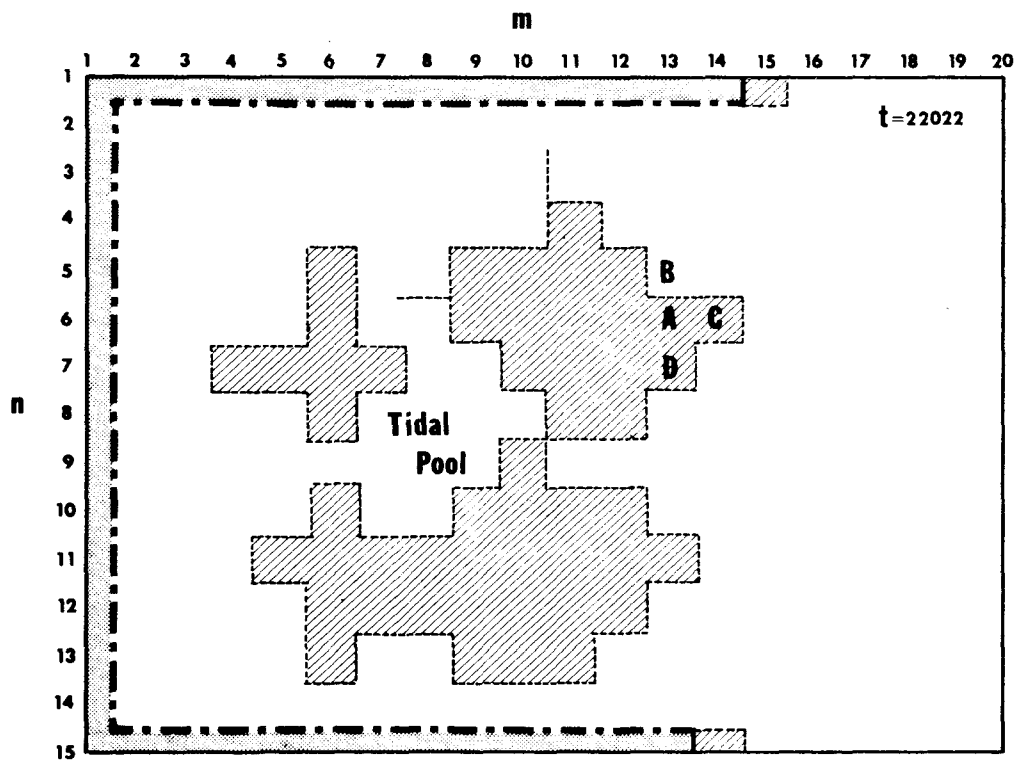


Figure 22. Maximum seaward advance of tidal flat F234.

THERMAL ADVECTION EXTENSION

The tidal flat grid as presented in Figures 14 and 15 was selected for procedural testing of the thermal advection extension. TABLE 2 presents typical tidal flat grid and run specifications as before; however, the computational time step was longer than the 30 sec step for the usual HN runs and the "continuous" heat pollution source was begun at 1200 sec. The change in time step is due to the fact that the procedure is driven from data saved at 120 sec intervals during a prior HN computation of ζ , U and V. A time step of 120 seconds was selected when it was determined that differences from 240 second step computations were significant although not substantial.

Figure 23 presents the thermal advection plume, the region affected by the residual heated fluid, after 8 1/3 source hours (approximately one "tidal" cycle). The source is essentially a single cell source depending on extant quantity of heated fluid. Heat budget computations occur to derate the excess heat over all areas where excess heat exists considering output radiation flux, latent heat transfer and convective sensible heat loss. Some portions of the advected volume thereby lose all of the associated excess heat. Volumes which have become associated with zero excess heat units, i.e., have been reduced to ambient temperature, are removed from the advection computation to become part of the background ambient volume. This occurs most noticeably over regions where volumes are spread over the tidal flat. The plume is thus split by the emergence of the tidal flat. Over several cycles the resulting plume "cast-offs" should be completely derated to ambient (based on observed numerical rates of cooling) or pass through the region boundary (lost to the computation in either case). These computational results seem reasonable in spite of the assumptions of no diffusion and no density dynamic effects.

MONTE CARLO DIFFUSION EXTENSION AND COMPARISON

The tidal flat grid as presented in Figures 14 and 15 was selected for procedural verification of the Monte Carlo extension. TABLE 2 presents typical tidal flat grid and run specifications as before. Here the Monte Carlo technique was employed as a special feature during computation of ζ , U and V, rather than as an after the fact procedure like the thermal advection extension. Four "continuous" Monte Carlo sources were started simultaneously at 1200 sec during an HN run from 0 to 31200 sec.

Figure 23 presents the Monte Carlo "plume," the approximate location of 4000 tracer points, after 8 1/3 hours (approximately one "tidal" cycle). Note the strong relationship of the Monte Carlo sources to the thermal advection source and strong correlation of the two "plumes." In spite of the difference in time step, the fact of the randomized diffusive effects in the Monte Carlo scheme, and the slight difference in the effective center of the two source types, the two methods gave distributions with very strong resemblance. The region where the separation occurs in the thermal advection plume is associated with a region of very low density of Monte Carlo points.

The "holes" which appear in the Monte Carlo distribution are an artifact of the separation of the four continuous point sources which were designed to present the outlines of a single cell source similar to the thermal advection

source. The triangular shape of the Monte Carlo distribution is the result of the divergence caused by the two exits to the tidal pool presented in Figure 22.

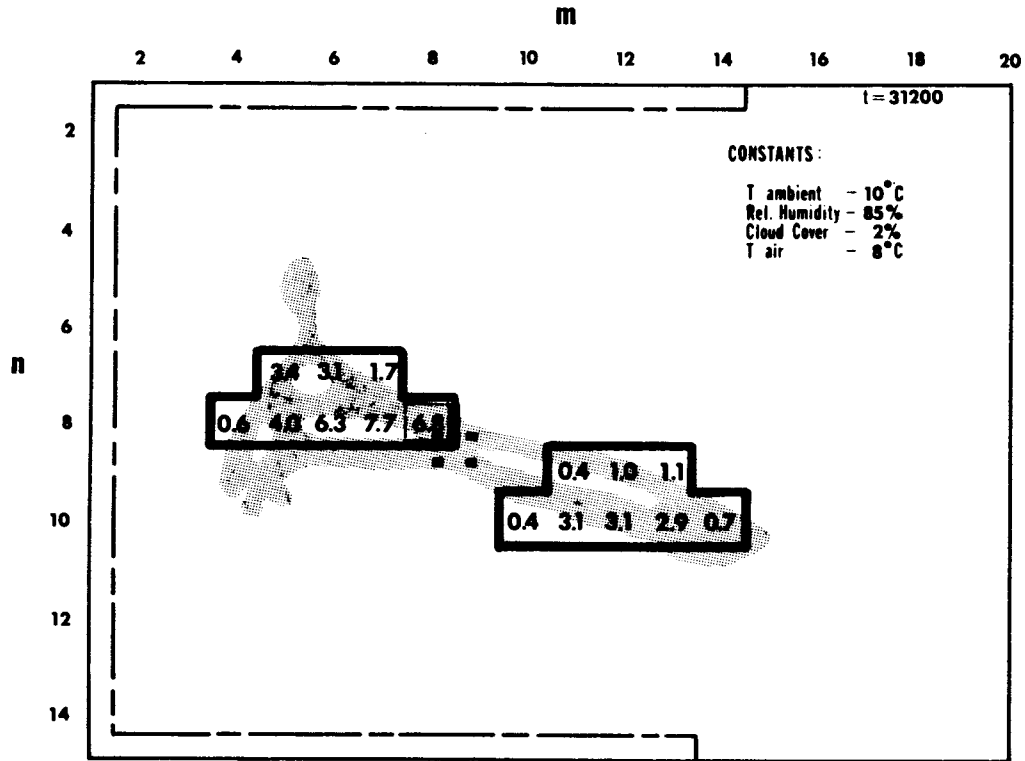


Figure 23. TFC continuous source "plumes."

REFERENCES

1. Bauer, R. A. Description of the Optimized EPRF Multi-layer Hydrodynamical-Numerical Model. ENVPREDRSCHFAC Tech. Paper No. 15-74, Environmental Prediction Research Facility, Monterey, California, 1974. 66 pp.
2. Hansen, W. Tides. In: The Sea, Vol. I, M. N. Hill, ed. Interscience Publishers, London, U.K., 1963. pp. 764-801.
3. Hansen, W. Hydrodynamical Methods Applied to Oceanographic Problems. In: Proceedings of the Symposium on Mathematical-Hydrodynamical Methods of Physical Oceanography, Institut Für Meereskunde der Universität Hamburg, Hamburg, West Germany, 1962. pp. 25-34.
4. Laevastu, T. and P. Stevens. Applications of Numerical-Hydrodynamical Models in Ocean Analysis/Forecasting. FNWC Tech. Note No. 51, Fleet Numerical Weather Central, Monterey, California, 1969. 70 pp.
5. Laevastu, T. and K. Rabe. A Description of the EPRF Hydrodynamical-Numerical Model, NEVPREDRSCHFAC Tech. Paper No. 3-72, Environmental Prediction Research Facility, Monterey, California, 1972. 49 pp.
6. Laevastu, T. A Vertically Integrated Hydrodynamical-Numerical Model (W. Hansen Type), Model Description and Operating/Running Instructions. Part I of a series of four reports. ENVPREDRSCHFAC Technical Note No. 2-74, Environmental Prediction Research Facility, Monterey, California, 1974. 63 pp.
7. Laevastu, T. A Multilayer Hydrodynamical-Numerical Model (W. Hansen Type), Model Description and Operating/Running Instructions. Part 2 of a series of four reports. ENVPREDRSCHFAC Technical Note No. 2-74, Environmental Prediction Research Facility, Monterey, California, 1974. 54 pp.
8. Laevastu, T. in collaboration with M. Clancy and A. Stroud. Computation of Tides, Currents and Dispersal of Pollutants in Lower Bay and Approaches to New York with Fine and Medium Grid Size Hydrodynamical-Numerical Models. Part 3 of a series of four reports. ENVPREDRSCHFAC Technical Note No. 3-74, Environmental Prediction Research Facility, Monterey, California, 1974. 51 pp.
9. Laevastu, T. and R. Callaway in collaboration with A. Stroud and M. Clancy. Computation of Tides, Currents and Dispersal of Pollutants in New York Bight from Block Island to Atlantic City with Large Grid Size, Single and Two-Layer Hydrodynamical-Numerical Models. Part 4

- of a series of four reports. ENVPREDRSCHFAC Technical Note No. 4-74, Environmental Prediction Research Facility, Monterey, California, 1974. 79 pp.
10. Leendertse, J. J. Aspects of a Computational Model for Long-Period Water-Wave Propagation. USAF Project RAND Memorandum RM-5294-PR, the RAND Corporation, Santa Monica, California, 1967. 165 pp.
 11. Laevastu, T. and G. D. Hamilton. Computations of Real-Time Currents Off Southern California With Multilayer Hydrodynamical-Numerical Models with Several Open Boundaries. ENVPREDRSCHFAC Technical Paper No. 10-74. 72 pp.
 12. Laevastu, T. and A. D. Stroud. Exchange between Coastal and Continental Shelf Waters as Computed with a Two-Layer HN Model, Manuscript Report, ENVPREDRSCHFAC Report to the Environmental Protection Agency, Corvallis Environmental Research Laboratory, Environmental Prediction Research Facility, Monterey, California, 1975.
 13. Lamb, H. Hydrodynamics. DOVER Publications, New York, New York, 1945. 738 pp.
 14. Laevastu, T. Multilayer Hydrodynamical-Numerical Models. In: Proceedings of the Symposium on Modeling Techniques, Am. Soc. Civil Engineers, San Francisco, California, 1975. pp. 1010-1025.
 15. Kagan (Cohen), B. A. Properties of Certain Difference Schemes Used in the Numerical Solution of the Equations for Tidal Motion. IZVESTIA, Atmospheric and Oceanic Physics, 6(7):704-717, 1970. Translated by F. Goodspeed.
 16. Pedersen, L. B. and L. P. Prahm. A Method for Numerical Solution of the Advection Equation $\partial C / \partial t = -\underline{V} \cdot \underline{\nabla} C$, Meteorological Institute of Denmark, as submitted to TELLUS, August, 1973. 36 pp.
 17. Laevastu, T. and J. M. Harding. Numerical Analysis and Forecasting of Surface Air Temperature and Water Vapor Pressure. Journal of Geophysical Research, 79(30):4478-4480, 1974.
 18. Laevastu, T., K. Rabe and G. D. Hamilton. The Effects of Oceanic Fronts on Properties of the Atmospheric Boundary Layer. ENVPREDRSCHFAC Technical Paper No. 2-72, Environmental Prediction Research Facility, Monterey, California, 1972.
 19. Laevastu, T. Factors Affecting the Temperature of the Surface Layer of the Sea, Soc. SCIENT, FENNICA, Comment, Physico-Mathem., Helsinki, 1960. 136 pp.
 20. Young, Chen-Shyong. Thermal Discharges into the Coastal Waters of Southern California. Southern California Coastal Water Research Project (SCCWRP), Los Angeles, California, 1971. 30 pp.

21. Maier-Reimer, E. Numerical Treatment of Horizontal Diffusion and Transport Phenomena in Marine Basins of Large Size, Institut für Meereskunde der Universität Hamburg, Hamburg, West Germany, as presented at IAMP/IASO Assembly, Melbourne, Australia, January, 1974.
22. Thompson, R. Numerical Calculation of Turbulent Diffusion. Quart. J. R. Met. Soc. 97(411):93-98, 1971.
23. Intersea Research Corporation. Semiannual Report of San Onofre Oceanographic and Biological Monitoring Program--July 1972-January 1973, prepared for Southern California Edison Company. La Jolla, California, August, 1973. pp. 1-7, 17-30, 190-196.

APPENDIX A

VERIFICATION OF THE MODEL

After the development of the various enhancements on the model using dummy data sets to test the code an attempt was made to verify the model using a real data case. Since data for the San Onofre Nuclear Power Station are reported to the San Diego Region Water Quality Control Board and were readily available, these data were selected for the test. Data are collected for San Onofre on a bimonthly schedule and are reported semi-annually. For 2 August 1972 the report (23) provides the tide curve, intermittent drogue measurements from 0800 to 1200 PDT, three infrared overflights, periodic wind measurements and bathythermograph measurements. During this period the plant was reported to be operating normally pumping 350,000 gallons of cooling water per minute and raising the temperature approximately 10°C.

MODEL SPECIFICATIONS

A single layer 20 by 40 HN grid with 500' mesh size oriented with the major axis along the coast was used to cover the San Onofre outfall region as shown in Figure A-1. Depths were interpolated to tenths of feet based on a bathymetric chart showing 6 foot depth contours from mean lower low water. An average latitude of 33°22'30"N was used to determine the mean gravitational constant and the mean coriolis effect over the grid. The usual bottom friction coefficient of .003 and a smoothing coefficient of .99 were used. The maximum depth at approximately 50 feet and the selected grid size resulted in a maximum time step for the HN scheme of 8 seconds through the CFL stability criterion.

The tides for the region were computed using the four major tidal constituents for the area, K1, O1, M2 and S2, adjusted for time and position. The tidal components were specified at three separate points on the seaward open boundary with temporal separation so that the tidal wave would propagate in the longshore direction toward the northwest. All additional points along the seaward boundary between the computed values were specified by linear interpolation. The tidal curve is shown in Figure A-2.

The southeastern and northwestern open boundaries to the region were not specified from external data except at the intersections of these boundaries with the seaward boundary. Heights at these boundaries were based solely on the dynamic boundary conditions. Observed wind values given in Figure A-2 were specified as uniform wind fields over the entire grid. The cooling water flow rate was used to define a "source" at the outfall positions and a "sink" at the intake position throughout the dynamic computations.

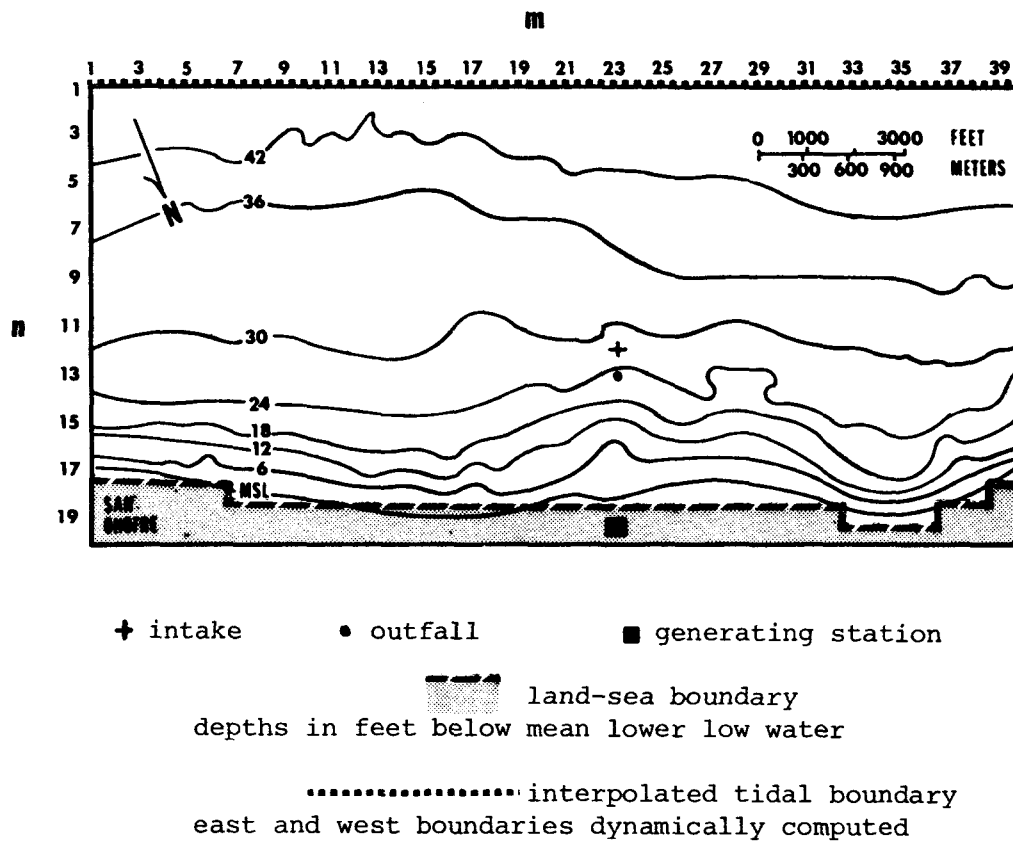
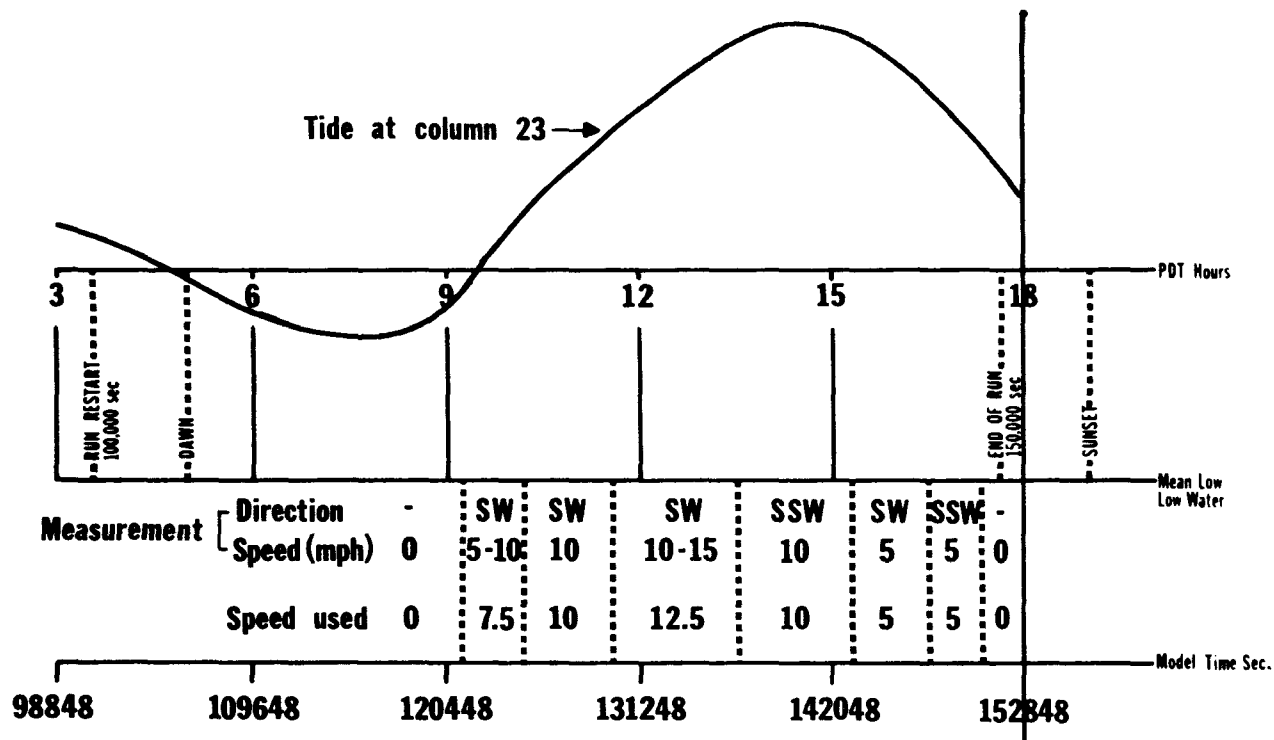


Figure A-1. San Onofre outfall area grid bathymetry.



Tide at column 23 was computed from MONACO constituents using an offset of 160345 seconds.

The tide at column 1 leads column 23 by 260 seconds.

The tide at column 40 lags column 23 by 209 seconds.

Tides were prescribed at points 2-22 and 24-39 by linear interpolation.

Figure A-2. San Onofre outfall tidal and wind prescription August 2, 1972.

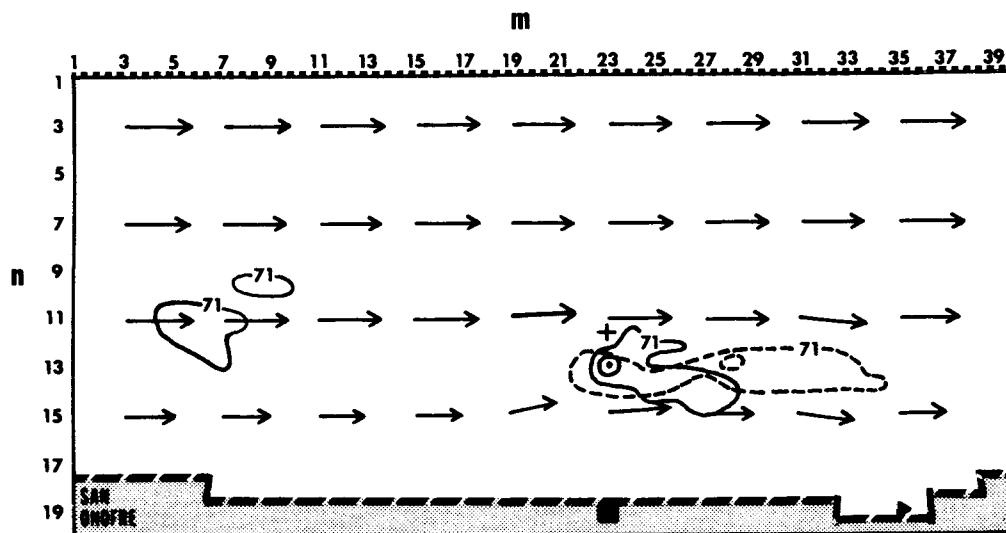
Both the non-linear and layer disappearance enhancements were used to simulate the dynamics for the region. No estimate was made of the impact of the non-linear terms on the computation; however, it was noted that the layer disappearance impact was minimal. The dynamic computations were initiated one full tidal cycle prior to the simulation date to assure prior proper convergence of the dynamic solution prior to application of the currents to drive the thermal advection problem. Data were saved at 120 second intervals during the dynamic computations for the thermal advection problem.

The time required to digitize the bathymetry, set up the control cards, verify the Phase I results and run the Phase II model was less than two man days. The Phase II model was stopped after each 25,000 second period out to 100,000 seconds to examine the results and then the model was restarted. As shown in Figure A-2 the model was then run for the tidal cycle that matched the 2 August conditions.

The integrated velocities calculated during the period of the drogue measurement agreed with the velocities measured by the drogues set at a depth of 15 feet. The calculated velocity pattern is shown in Figure A-3. The velocities are between 35 and 40 cm/sec while the drogues had velocities of between 35 and 43 cm/sec with both showing the characteristic movement along shore to the northwest during the period of rising tide. Figures A-4 and A-5 show lower velocities and finally the reversal inshore as the tide reaches a maximum and begins to ebb.

THERMAL ADVECTION

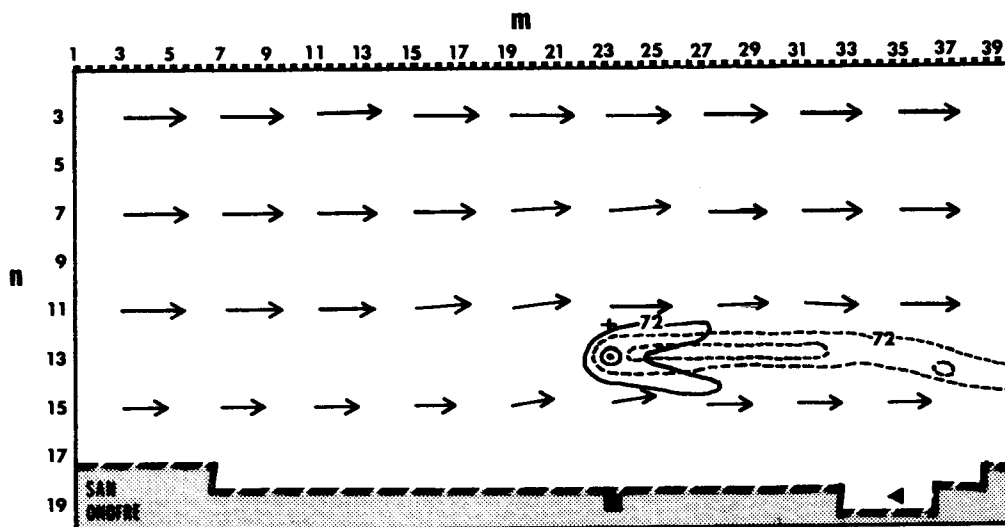
The velocity fields saved from the Phase II model at 120 second intervals were used for the thermal advection model run beginning at the model time equivalent to 2022 PDT on 1 August 1972. Figures A-3 through A-5 show the plume 15, 17 and 19 hours after the start and compare the computed plume to the infrared measurements. Only two contours are compared for each figure, a contour 1°C (1.8°F) above ambient temperature and a contour 6.56°C (11.8°F) above ambient. The computed values show the highest values downstream in the plume rather than the "bubble" over the outfall. Since diffusion was not considered horizontally or vertically, no spreading of the heat to surrounding waters occurs. The hottest portions of the computed plume passed back and forth over the outfall as the tidal currents reversed receiving a double dose of heating. Even though the radiation terms in the model were reducing the heat content of this water, the limited surface exposed did not produce sufficient cooling. The temperature of the plume did not drop to the level of the background temperature within the area modelled as expected. Several minor fixes were attempted to improve the agreement between the observed and modelled results by modifying the widths of the heated portions of the cells and changing constants in the radiation equations but all attempts simply showed that the numbers obtained reflected the basic assumption of pure advection and that a major effort beyond the scope of the previous tasks would be required to adequately include diffusion in the model.



Contours: 21.7°C (71.0°F) and 27.2°C (81.0°F). Ambient: 20.7°C (69.2°F).

——infrared -----computed → 50 cm/sec

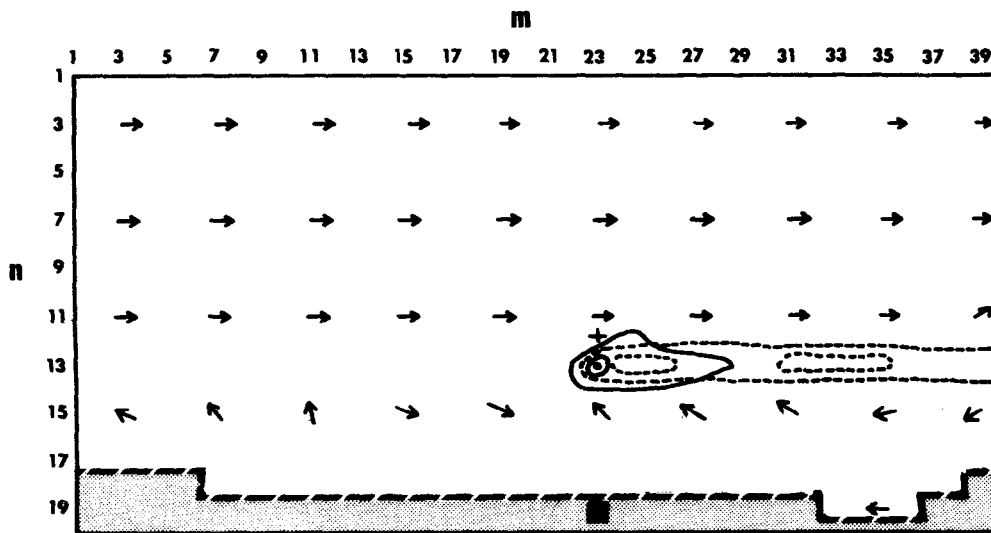
Figure A-3. Infrared flight 0958-1107 compared to values after 15 source hours.



Contours: 22.2°C (72.0°F) and 27.7°C (82.0°F). Ambient: 21.2°C (70.2°F).

——infrared -----computed → 50 cm/sec

Figure A-4. Infrared flight 1226-1344 compared to values after 17 source hours.



Contours: 22.5°C (72.5°F) and 28.1°C (82.5°F). Ambient: 21.5°C (70.7°F).

——infrared - - - - - computed → 50 cm/sec

Figure A-5. Infrared flight 1503-1617 compared to values after 19 source hours.

TECHNICAL REPORT DATA
(Please read Instructions on the reverse before completing)

1. REPORT NO. EPA-600/3-78-073		2.	3. RECIPIENT'S ACCESSION NO.
4. TITLE AND SUBTITLE Enhanced Hydrodynamical-Numerical Model For Near-Shore Processes		5. REPORT DATE July 1978	
		6. PERFORMING ORGANIZATION CODE	
7. AUTHOR(S) R.A. Bauer and A.D. Stroud		8. PERFORMING ORGANIZATION REPORT NO.	
9. PERFORMING ORGANIZATION NAME AND ADDRESS Compass Systems, Inc. San Diego, California 92109		10. PROGRAM ELEMENT NO. EHE 625	
		11. CONTRACT/GRANT NO. 68-03-2225	
12. SPONSORING AGENCY NAME AND ADDRESS Environmental Research Laboratory-Corvallis Office of Research and Development U.S. Environmental Protection Agency Corvallis, Oregon 97330		13. TYPE OF REPORT AND PERIOD COVERED final 1975-1977	
		14. SPONSORING AGENCY CODE EPA/600/02	
15. SUPPLEMENTARY NOTES			
16. ABSTRACT An optimized version of a multilayer Hansen type Hydrodynamical-Numerical (HN) model is presented and discussed here as the basis for the following experimental extensions and enhancements developed to more appropriately handle near-shore processes: <ul style="list-style-type: none"> •Non-linear term extension to facilitate small-mesh studies of near-shore, including river inflow dynamics; •Layer disappearance extension to enable appropriate procedures in tidal flat and marshy regions, as well as some down/upwelling cases; •Thermal advection enhancement for treatment of thermal pollution cases by method of moments coupled with heat budget procedures for dynamic plume development experiments; •Monte Carlo diffusion enhancement to deal with dispersion via statistical methods and comparison to the method of moments experiments. Extensive efforts were invested in determining reasonable and appropriate boundary conditions for both the basic model and the extended versions presented here.			
17. KEY WORDS AND DOCUMENT ANALYSIS			
a. DESCRIPTORS		b. IDENTIFIERS/OPEN ENDED TERMS	c. COSATI Field/Group
numerical methods marshy regions thermal pollution operations research monte carlo methods mathematical methods near-shore river inflow tidal flat			08/C 12/A,B
18. DISTRIBUTION STATEMENT Release to Public		19. SECURITY CLASS (This Report) Unclassified	21. NO. OF PAGES 70
		20. SECURITY CLASS (This page) Unclassified	22. PRICE